

Greenland Ice Sheet Surface Melt and Its Relation to Daily Atmospheric Conditions

RICHARD I. CULLATHER ^{a,b}

^a *Earth System Science Interdisciplinary Center, University of Maryland at College Park*

^b *Global Modeling and Assimilation Office, NASA Goddard Space Flight Center,
Greenbelt, Maryland*

AND

SOPHIE M.J. NOWICKI ^c

^c *Cryospheric Sciences Laboratory, NASA Goddard Space Flight Center, Greenbelt, Maryland*

Submitted to: *Journal of Climate*

June, 2017

Revised

November, 2017

Corresponding author address: Richard Cullather, % NASA/GSFC Code 610.1,
8800 Greenbelt Road, Greenbelt, MD 20771.

E-mail: richard.cullather@nasa.gov

ABSTRACT

Melt area is one of the most reliably monitored variables associated with surface conditions over the full Greenland Ice Sheet (GrIS). Surface melt is also an important indicator of surface mass balance and has potential relevance to the ice sheet's global sea level contribution. Melt events are known to be spatially heterogeneous and have varying time scales. To understand the forcing mechanisms, it is necessary to examine the relation between the existing conditions and melt area on the time scales that melt is observed. Here, we conduct a regression analysis of atmospheric reanalysis variables including sea level pressure, near-surface winds, and components of the surface energy budget with surface melt. The regression analysis finds spatial heterogeneity in the associated atmospheric circulation conditions. For basins in the southern GrIS, there is an association between melt area and high pressure located south of the Denmark Strait, which allows for southerly flow over the western half of the GrIS. Instantaneous surface melt over northern basins is also associated with low pressure over the central Arctic. Basins associated with persistent summer melt in the southern and western GrIS are associated with the presence of an enhanced cloud cover, a resulting decreased downwelling solar radiative flux, and an enhanced downwelling longwave radiative flux. This contrasts with basins to the north and east, where an increased downwelling solar radiative flux plays a more important role in the onset of a melt event. The analysis emphasizes the importance of daily variability in synoptic conditions and their preferred association with melt events.

1. Introduction

The Greenland Ice Sheet (GrIS) represents a significant store of freshwater which may be intermittently released into the global ocean. Recent studies using satellite-derived mass change have indicated the GrIS has made a substantial contribution to global sea level in the past decades (Shepherd et al. 2012). Historically, it has been thought that this contribution has been equally divided between iceberg calving and surface processes (e.g., van den Broeke et al. 2009). Observed, enhanced surface melt over the GrIS in the past decade has led to an increased focus on surface mass balance (SMB) and an identification of surface melt as having a dominant role in the contribution of the ice sheet to sea level rise (Rignot et al. 2011; Velicogna et al. 2014; Enderlyn et al. 2014; van den Broeke et al. 2016).

Arguably, the most consistent and reliable source of surface melt data encompassing the full GrIS is passive microwave data. The MEaSUREs (NASA Making Earth System Data Records for Use in Research Environments program) daily surface melt product (Mote and Anderson 1995; Mote 2007) covers the full ice sheet with a grid spacing of 25 km. These data have been used to document the recent, enhanced melt over the last decade, including the 11-July 2012 event in which nearly the entirety of the GrIS experienced melt conditions. It is of interest to understand the conditions and processes that are associated with enhanced melt events that are documented in these data. Previous studies have focused on the presence of intense North Atlantic atmospheric blocking events (e.g., Rajewicz and Marshall 2014, Häkkinen et al. 2014; McLeod and Mote 2016). These conditions may preferentially allow for an enhanced solar radiative flux to reach the ice sheet surface and allow for albedo feedback processes to promote large-scale melting. Alternatively, Bennarz et al. (2013) identified the importance of warm air advection and the role of clouds in communicating melt energy to the ice sheet surface via

increased downwelling longwave fluxes. Recently, Tedesco et al. (2016a) noted the role of Arctic high pressure systems in producing increased melt over the northern regions of the GrIS during the 2016 season. The large-scale atmospheric circulation may produce increased melt by providing cloudless conditions which enhance solar radiation, by the advection of warm air over the ice sheet (Fettweis et al. 2011), by providing moisture and cloud cover which alters downwelling infrared flux properties, and/or by influencing turbulent fluxes and surface winds. It is widely acknowledged that the GrIS climate experiences considerable spatial variability (e.g., Chen et al. 1997, Vernon et al. 2013, Velicogna et al. 2014). The geographical proximity of an ice sheet location to anomalous circulation may produce localized conditions which enhance or inhibit melt.

It is of interest to understand the conditions present during extreme melt events and identify how the conditions vary regionally across the ice sheet. In this study, the daily MEaSUREs data set is examined in relation to concurrent conditions using a simple linear regression analysis. The conditions are examined regionally by using defined GrIS basins. Atmospheric general circulation and cloud conditions are described using the Modern-Era Retrospective analysis for Research and Applications, version 2 (MERRA-2). Section 2 provides a description of the data sets used and the regression method. In section 3, a discussion of general circulation, energy budget components, and temperature fields regressed against observed melt area is provided. Anecdotal case studies are given in section 4, which provide additional insight into the determined patterns. A discussion and summary is given in section 5.

2. Data sets and method

MERRA-2 is a global atmospheric reanalysis produced by the NASA Global Modeling and Assimilation Office for the period from 1980 to the present (Gelaro et al. 2017; GMAO 2015a,b,c,d). The output fields are produced in hourly averaged fields at $\frac{1}{2}^{\circ}$ latitude by $\frac{5}{8}^{\circ}$ longitude for surface flux and single level fields. For this study, the hourly fields are averaged to produce daily output. MERRA-2 represents an update of the original MERRA system (Rienecker et al. 2011) and includes improvements made to the data assimilation system and background model (Molod et al. 2015). The prognostic cloud cover simulates large-scale condensation, evaporation, autoconversion, and accretion of cloud water and ice, sedimentation of cloud ice, and re-evaporation of falling precipitation (Molod et al. 2012; Bacmeister et al. 2006). Terrestrial and solar radiative processes are described by Chou and Suarez (1994, 1999). Over polar ice sheets, the surface representation has been updated to provide a prognostic snow albedo (Greuell and Konzelman 1994), improve the representation of surface energy conductivity, and represent snow hydrology processes including compaction, meltwater percolation, refreezing, and runoff (Cullather et al. 2014).

The MEaSUREs daily melt fields were obtained from the US National Snow and Ice Data Center for the available period 1980-2012, and are provided on the Equal Area Scalable Earth Grid 2.0 (EASE-2; Mote 2014). The data are derived from available SMMR, SSM/I and SSMIS radiances after Mote and Anderson (1995). The data are available on alternating days for the SMMR instrument period prior to 9-July 1987, and daily thereafter. Surface melt is determined via comparison of 37GHz, horizontally polarized brightness temperatures with dynamic thresholds generated by a microwave emission model.

For this study, the daily melt area is summed over major GrIS basins defined by Zwally et al. (2012), producing a time series of summed daily melt area normalized by the size of each basin. A subset of the time series is taken in which melt area is greater than 5 percent of the basin area. This limits the regression analysis to the melt season and the relation of melt to conditions that are concurrently observed, while maintaining a large sample size. An average of 1000 days over the 33 year period are available for each basin. Concurrent MERRA-2 anomalies were computed by subtracting the calendar day mean for the 1980-2010 period. The least-squares linear trend was then removed from the anomaly fields. Linear regression coefficients were then computed using the melt area time series and concurrent MERRA-2 anomaly variables at each grid point. The coefficients are expressed as the units of the MERRA-2 variable per total area of the basin. The uncertainty in the regression is indicated using the student's t-statistic at the 99 percent confidence level. Field significance (e.g., Livezy and Chen 1983) for select, representative variables (sea level pressure, skin temperature, and cloud fraction) was evaluated via a Monte Carlo procedure. For the procedure, the regression analysis is recursively computed using a randomized ordering of the melt area time series. The area of statistical significance is then computed for each iteration. Using northern and southern basin melt areas (basins 1 and 5 indicated on Fig. 1) regressed against MERRA-2 for the region poleward of 50°N, the unrandomized regression area of significance was found to be within the 95 percent confidence of the Monte Carlo distribution. While field significance has not been assessed for all results shown, it is also important to consider results in the context of the physical processes involved. This serves as an additional motivating factor in examining individual ice sheet melt events in more detail.

Figure 1 shows the major drainage basins as defined by Zwally et al. (2012), which are widely used in literature (e.g., Seo et al. 2015, Colgan et al. 2015). The basins range in size from 51,000 km² for basin 5 in the south to 326,000 km² for basin 2 in the northeast. A typical sample of the time series of daily surface melt is shown in Fig. 1(b). Each time series of melt area has been normalized by the total basin area. It may be seen that the time series contains high temporal variability and that events occur on short time scales. On average there is a defined seasonal cycle with larger values in summer. But the time series of an individual year is not necessarily sinusoidal, and significant departures may occur (e.g., Cullather et al., 2016). There are periods where several basins or even the total ice sheet is responding similarly, such as during July 2012. At other times, however, the observed melt area is localized. Over the full 1980-2012 period, Table 1 presents correlations of these time series. The temporal variability of melt area in adjacent basins tends to be better correlated, such as basin 1 and basin 2 in the north and northeast, and basins 5 and 6 in the south and southwest. The correlation between northern and southern basins tends to be lower. This may be reflective of the different character of the time series shown by Cullather et al. (2016), in which melt in the southern GrIS tends to be more episodic. Western basins are generally well correlated with melt over the total GrIS. Basin 5 in the south, which experiences the most frequent melt, is less correlated with the total GrIS melt area.

3. Results

Results of the regression analysis are given below for MERRA-2 variables associated with atmospheric circulation, clouds and surface radiative flux variables, and near-surface winds.

Anecdotal case studies of historical GrIS melt events using the determined relations are then presented.

a. General Circulation

Figure 2 shows spatial patterns of regression of MERRA-2 skin temperature against the summed passive microwave melt area. For each map, the green outline denotes the basin over which melt area values were computed. These area values are then regressed against the MERRA-2 fields. As noted in Hall et al. (2009), skin temperature is closely related to the presence of surface melt, and the regression maps reflect this correspondence. The analysis denotes simultaneous skin temperature anomalies at individual locations for surface melt occurring within the basin highlighted in green. Melt occurring throughout the entirety of the GrIS (center map) is associated with significant, positive temperature anomalies over most locations, but particularly large values at interior locations over the western and southern regions of the ice sheet, where melt occurs more frequently. For southern basin 5, locations within its boundary are associated with positive skin temperature anomalies of up to 6°C. Locations within basin 5 that are farther inland are found to be associated with larger anomalies, which conforms to a climatology of decreasing temperatures with elevation and the necessity of a larger temperature anomaly in order to produce melt. Locations at lower elevations that frequently experience melt are associated with smaller temperature anomalies. Thus the basin geometry plays a key role in the realized patterns. Similarly, the magnitude of skin temperature anomalies determined from regression using southern basins is generally smaller than is shown for regression maps of melt area in northern basins. The regression maps shown in Fig. 2 broadly reflect correlations between basins that are indicated in Table 1. Surface melt area for basin 5 is correlated with melt area in

adjacent basins 4 and 6. Positive temperature anomalies are shown for these locations in the regression map for basin 5; for the northern areas of the GrIS, the regression values are smaller and there is no statistical significance. Melt occurring in eastern basin 3 is associated with large temperature anomalies occurring over the central part of the GrIS. This implies that melt occurring in basin 3 is associated with conditions affecting a region larger than the size of the basin. Regression patterns for southern basins 4, 5, and 6 are more localized than for northern basins 2 and 8 and for central basins 3 and 7. Temperature anomalies associated with basin 1 are also more localized than adjacent basins.

Figure 3 similarly presents the spatial regression patterns of surface melt area for each basin with MERRA-2 500 hPa geopotential height anomalies. Daily melt area over the total GrIS is associated with significant positive height anomalies over Greenland, centered in the southeastern part of the island, a pattern in agreement with the analysis of Häkkinen et al. (2014) for the 2000-2013 MODIS period (MODIS: Moderate-resolution imaging spectroradiometer). For regression maps of individual basins, the patterns of height anomalies differ depending on the basin geography. Southern basins 4, 5, and 6 are associated with positive height anomalies occurring in a localized area south of the Denmark Strait. This would suggest anticyclonic flow around the height anomaly, producing southerly advection over the southern half of the GrIS. Regression maps for eastern basin 3 over the central latitudes of the ice sheet indicate the center of the height anomaly is displaced northward and to the northwest of Iceland. The regression pattern for basin 7 is similar to that of basin 3 but with the height anomaly located slightly to the south and west. The regression map for northeastern basin 2 shows positive height anomalies over the basin and centered along the southern boundary, but a negative height anomaly over the central Arctic Ocean is also indicated. The only basin regression indicating a height anomaly

centered over the western side of the ice sheet is basin 1. This pattern is more consistent with an eastward advection into the basin 1 region. For northern basins, the regression maps generally indicate negative height anomalies over the British Isles and Scandinavia. For each of the basins shown in Fig. 3, locations within the basin itself are associated with positive height anomalies.

Figure 4 shows corresponding patterns for MERRA-2 sea level pressure. In general, there is uncertainty in numerical analyses associated with the reduction of surface observations to sea level in locations of high topography which must be kept in mind; this corresponds to places over the central GrIS. In Fig. 4 there is a considerable amount of correspondence between the regression patterns in sea level pressure and for 500 hPa geopotential height anomalies shown in Fig. 3. This suggests an equivalent-barotropic structure in the anomaly patterns, which is associated with atmospheric blocking events (e.g., Frederiksen and Bell 1990; Davini et al. 2014). The pattern is readily seen for southern basin regression maps in which positive pressure anomalies are co-located with positive values in the height field. For basins 1, 3, 7, and 8, the geopotential height anomaly shown in Fig. 3 is located over the ice sheet surface. The sea level pressure regression patterns shown in Fig. 4 are partially obstructed by the ice sheet surface, but for locations beyond the ice sheet periphery there is general agreement between the height and sea level pressure patterns. The regression pattern of sea level pressure anomalies for northeastern basin 2 differs from the corresponding geopotential height field regression in several aspects. The pressure anomalies for locations within the basin are negative as compared to positive values in the height field. This is true even for coastal locations in the basin at low elevation. The sea level pressure regression pattern for basin 2 indicates no positive anomalies within proximity of the ice sheet. The regression field also does not reflect the positive height

values over southern Labrador found in the corresponding 500 hPa height anomaly regression shown in Fig. 3.

The importance of the positive pressure values southeast of the GrIS is partly conveyed by the regression patterns associated with temperature anomalies in the free atmosphere. Corresponding patterns for MERRA-2 700 hPa temperature are shown in Fig. 5. The regression pattern for the total GrIS and for most of the individual basins indicate a positive temperature anomaly centered to the eastern side of the ice sheet. These areas correspond to the location of greatest disruption in the North Atlantic baroclinic flow imposed by the blocking height anomalies. Positive temperature anomalies overlie each basin in the analysis.

Recent studies have suggested a relation between GrIS surface conditions and adjacent sea ice cover (e.g., Rennermalm et al. 2009, Liu et al. 2016, Hanna et al. 2014, Noël et al. 2014). Summertime Arctic ice cover has trended significantly lower in recent years, concurrent with increased GrIS surface melt. While enhanced melt cover in northern and western basins is associated with a reduced sea ice concentration in adjacent areas (not shown), a cause-and-effect relation is not supported through regression analysis alone.

b. Cloudiness and surface radiative fluxes

Figure 6 indicates regression patterns associated with the MERRA-2 surface downwelling longwave radiative flux. As with surface temperature, the anomalies are positive and significant within each basin considered, and the spatial maxima in the patterns is generally located within the boundaries of the basin. For the entirety of the GrIS, the regression pattern indicates larger anomalies located to the west of the center of the ice sheet. Smaller values between 40 and 60 W m⁻² are found in the southwestern GrIS, while values less than 40 W m⁻² are found in the

northeast. The magnitudes of the longwave anomalies are larger for central basins 3 and 7, and for northwestern basin 8. For these basins, anomalies are locally greater than 60 W m^{-2} , while anomalies are less for southern and northeastern basins.

The surface downwelling shortwave radiative flux regression maps shown in Fig. 7 contrast with the longwave in showing both significant positive and negative anomalies over large areas of the ice sheet. For the full GrIS, the regression indicates positive anomalies over the eastern side, with values of up to 45 W m^{-2} , which increase in magnitude toward the coast. Along the western side of the GrIS, the regression values are negative with magnitudes of up to $(-) 50 \text{ W m}^{-2}$ along the western periphery. Negative values also encompass the southern edge of the ice sheet. In the regressions for each basin, enhanced melt area is associated with a decreased downwelling solar flux within the basin for southern basins 4, 5, and 6 and western basins 7 and 8. There is an indication of a topographical influence on the western basin regressions, with values becoming smaller at higher elevation. This is particularly true in the vicinity of South Dome. For northern basin 1, the values are generally negative within the boundaries, although the significance is less uniform. The magnitudes shown are generally larger for regressions associated with the western basins, with values greater than $(-) 50 \text{ W m}^{-2}$, while the magnitude for basin 1 is generally less than 25 W m^{-2} . For northeastern basin 2, the analysis indicates small positive values within the basin domain of less than 40 W m^{-2} , which increase towards the coastline, and negative values in the northwest and southern regions of the ice sheet. But the field is not significant over most of the ice sheet. For eastern basin 3, values are small but mostly positive within the basin boundaries. There is an area of significant negative values along the southern edge of the basin. Beyond the boundaries of basin 3, there are significant positive values over the northeastern GrIS, and significant negative values to the southwest.

An enhanced downwelling longwave flux may result from the presence of emitting cloud water or ice, but also in the presence of advected warm air. In contrast, the presence of clouds during sunlit hours will invariably alter the downwelling shortwave flux. Thus the regression patterns for cloud fraction are expected to more closely resemble those of the shortwave flux shown in Fig. 7, except for in the presence of optically thin clouds. As shown in Fig. 8, the patterns of MERRA-2 total cloud fraction generally reflect the regression patterns for the downwelling shortwave flux shown in Fig. 7. For the regression over the total GrIS, enhanced melt area is associated with significantly less cloud cover in the northeastern GrIS, and more cloudiness in the western and southern GrIS. Differences in the patterns for Figs. 7 and 8 are associated with conditions that extend beyond the boundaries of basins for the melt area considered. Nevertheless the patterns are broadly similar.

c. Near-surface winds

The examination of regression patterns associated with circulation and radiative variables finds a contrast between general conditions promoting surface melt in the southern GrIS, where warmer temperatures are more common, and northern regions of the ice sheet. But a contrast is also found between western basins, where atmospheric moisture appears to play a significant role, and eastern basins, where localized, episodic conditions may be important. In particular, northeast basin 2 was found to have an association of less cloudy conditions with surface melt. These regions follow a characterization of near-surface winds given by Moore et al. (2013). Moore et al. (2013) identified a southerly near-surface plateau jet along the western side of the ice sheet in summer, and a distinct, westerly jet over the northeastern GrIS. A regression analysis of 10 m zonal and meridional components to the melt area is performed, and is shown in Fig. 9.

The regression patterns indicate the relation of southerly winds over the western two-thirds of the ice sheet to enhanced melt, which is consistent with the advection of atmospheric moisture over the western side of the ice sheet. The zonal wind regression indicates easterly near-surface winds over the southern third of the GrIS and westerly winds focused over the lower elevations of basin 3 on the eastern GrIS. These patterns are consistent with a terrain-following anticyclonic circulation centered to the southeast of the GrIS.

d. Case studies

Given these general characteristics from regression covering the full satellite era, examination of individual melt events provides illustrative information on the applicability of these patterns to given cases. While anecdotal, the cases include widely-studied and documented melt events that occurred on the GrIS.

The most significant melt event for the period investigated occurred on 11-July 2012, in which almost 90 percent of the ice sheet was simultaneously experiencing surface melt, including Summit. The 2012 event has been extensively studied (e.g., Nghiem et al. 2012; Bennartz et al. 2013; Tedesco et al. 2013; Fausto et al. 2016). The synoptic patterns associated with the event are shown in Fig. 10(a) and include a blocking surface high pressure centered to the west of Iceland, and strong southeasterly flow over the southern part of the ice sheet. Conditions were also characterized by extensive cloud cover over the southern and western areas of the ice sheet. While melt over most of the GrIS was reduced in the ensuing days, a large area of surface melt over northern basin 1 persisted for the following 5 days. This period was associated with a low pressure system over the Arctic Ocean, to the north of the GrIS. The

reanalysis also indicates cloud cover over most of the ice sheet during the day of largest melt area, in agreement with observations (Bennartz et al., 2013).

A significant event occurred over the period 14-19 July 1989, in which roughly 35 percent of the GrIS simultaneously experienced melt on 15-July. As seen in Fig. 11, the melt area is primarily located in the southern half of the GrIS. A broad high pressure system was located near Iceland but was centered to the southeast (Fig. 11). Nevertheless, southeasterly near-surface winds occurred over a large area of the southern GrIS where surface melt was detected. These areas were also associated with a high total cloud fraction, as seen in Fig. 11(b). Basins in the northern GrIS did not experience significant melt, and high pressure was located to the north over the Arctic Ocean.

On 12-August 1997, GrIS surface melt covered approximately 45 percent of the ice sheet, primarily covering southern and western basins 4, 5, 6, and 7 (Fig. 12). As seen in Fig. 12, localized anticyclonic circulation is found near and to the east of Cape Farewell on the day of greatest melt area, and near surface winds again show southeasterly flow across the southern tip of the GrIS.

Over the period June-July 2002, northeastern basin 2 experienced two melt events (Fig. 13). The first occurred on 29-June and was associated with significant melt over the entire GrIS. Greater than 70 percent of the ice sheet experienced melt over the period 28-29 June. As seen in Fig. 13, sea level pressure of greater than 1020 hPa was present to the south of Iceland. Near-surface wind flow from the southeast is found over the southern half of the ice sheet, and westerly flow is found over northeastern basin 2. A low pressure system was also present over the Arctic Ocean. On 14-July 2002, more than 70 percent of basin 2 experienced surface melt, in

contrast with other areas of the ice sheet. On this day, surface winds over basin 2 were directly from the south.

Tedesco et al. (2016) reviewed conditions for summer 2015 over the GrIS, in which anomalous, extensive surface melt in the northern regions of the ice sheet was present. Tedesco et al. (2016) associated these conditions with monthly-averaged high pressure anomalies over the central Arctic in summer, which promoted the advection of warm air from the east over northern basins. The year 2015 is not covered by the currently available MEaSUREs data set, however melt area may be approximated using the melting point in MERRA-2 skin temperature (e.g., Cullather et al. 2016). The resulting time series for summer 2015 shown in Fig. 14(a) indicates enhanced melt in northern basins 1 and 8 beginning on 2-July. The melt extent for basin 1 remains consistently high until 22-July. An examination of the prevailing daily conditions indicates a weak low pressure feature over the central Arctic at the beginning of the event (Fig. 14(b)), which generally provided westerly surface winds along the Arctic coast of the GrIS. Additional cyclonic circulation features passed along the northern GrIS coastline until 4-July, when high pressure begins to dominate the Arctic Ocean. As noted in Cullather et al. (2016), the temporal variability of the melt time series in northern basins is more muted than for elsewhere on the GrIS. A more persistent nature of melt in the northern basin may extend beyond the time scale for synoptic events and increase uncertainty in the regression analysis.

These five anecdotal events underscore the relation of high pressure in the vicinity of Denmark Strait and southeasterly flow to enhanced surface melt, particularly over southern basins. Enhanced daily surface melt area over northern basins has an association with low pressure systems over the Arctic Ocean, which appear to enhance westerly winds along the northern edge of ice sheet. Below, the significance of this association is discussed further. Two

significant melt events for northeastern basin 2 occurred in July 2002, but these events were dissimilar, suggesting varying mechanisms are responsible for melt.

4. Discussion

The novel aspects of this study have emphasized the consideration of both location and temporal scale in examining conditions that are associated with surface melt on the GrIS. The results shown indicate a general agreement with previous studies on the role of atmospheric blocking in enhancing surface melt (Häkkinen et al. 2014, Hanna et al. 2016, McLoud and Mote 2016), although spatial heterogeneity is also found in the location of pressure anomalies. The patterns have similarity with summertime teleconnection features (e.g., Folland et al. 2009). The circulation patterns also suggest a role of synoptic systems over the central Arctic in increasing melt area for the northern parts of the ice sheet. Synoptic low pressure systems over the central Arctic Ocean provide eastward advection across the northern GrIS, and enhance downslope winds in the northeastern basin. Regression patterns over other basins and for the full GrIS emphasize the role of clouds and enhanced moisture in communicating warmer air aloft to the surface. Melt area is enhanced in the presence of increased cloudiness and a large downwelling longwave radiative flux. This is consistent with the patterns described in Bennarz et al. (2013) and elsewhere concerning the role of mixed phase clouds in the Arctic (e.g., Kay et al. 2016; Van Tricht et al. 2016). In a recent study, Hofer et al. (2017) attributed recent reductions in GrIS SMB to a coincident trend in decreasing summer cloud cover, enhancing the melt-albedo feedback. MERRA-2 indicates a spatial pattern in the trend of seasonally-averaged summertime cloud fraction which compares closely to that shown for MODIS data in Hofer et al. (2017, their Fig. 1). The use of daily data in this study shows that decreasing seasonal-mean cloud fraction is

not associated with melt events in southern and western basins of the ice sheet. A possible explanation for the seasonally-averaged cloud fraction trend is that ambient temperatures are raised beyond the condensation point subsequent to a surface melt event. The analysis does not preclude prolonged surface mass loss via the ice/albedo feedback mechanism after the occurrence of large melt events, which rapidly alter surface properties including albedo (e.g., Tedesco et al. 2011, Tedesco et al. 2016b). While this study focused on satellite-derived melt area, Hofer et al. (2017) examined model-derived SMB. Surface melt is an important indicator of SMB, but models suggest that events in melt areal extent and events in SMB may differ (e.g., Cullather et al. 2016; Box et al. 2012). Nevertheless, the initial onset of a typical melt event in southern and western GrIS basins is found to be associated with enhanced rather than reduced cloudiness.

Similar to other models and analyses, the representation of MERRA-2 clouds is likely deficient in several aspects including phase and vertical structure. Lenaerts et al. (2017) examined reanalysis clouds against CloudSat-CALIPSO derived observations and found that MERRA-2 produces too many liquid-water clouds at the expense of ice clouds. Alternatively, Liu and Key (2016) found reanalyses including MERRA-2 exhibit some capability for reproducing mean cloud anomalies. The surface representation of the GrIS in MERRA-2 has previously been examined in comparison to in situ flux and temperature data (Cullather et al. 2014; Reeves Eyre and Zeng 2017). Nevertheless, the regression analysis presented here emphasizes the timing of atmospheric moisture and its co-location with enhanced melt. Over Greenland, reanalysis conditions are also locally constrained by the local rawinsonde network (e.g., Robasky and Bromwich 1994).

The results shown are generally found to be robust. For example, Fig. 15 shows the regression of melt area on sea level pressure as in Fig. 4, but restricted to years prior to 2000, in which surface melt was generally less than observed in the 21st Century. Figure 15 nevertheless indicates patterns that are similar to Fig. 4. In particular, the compact high pressure regression pattern south of Denmark Strait for southern basins 4-6 is similar in Figs. 4 and 15. The presence of a low pressure pattern over the central Arctic corresponding to basin 2 is also similar, though it is not significant for the earlier period. For northern basins 1 and 8, and for the regression using melt area for the total GrIS, the largest differences between the earlier period shown in Fig. 15 and the full time series shown in Fig. 4 are associated with the region to the north of the Canadian Arctic Archipelago. The patterns shown in Fig. 15 suggest a correlation with high pressure in the area, while the regression for the full available time period shown in Fig. 4 indicates regression values near zero and of no significance. These differences may be due to interannual variability, and the overall lack of melt events in these basins prior to the most recent decade. Similar Arctic circulation anomalies can produce markedly different air temperature anomalies (Serreze et al., 2016). Nevertheless, the agreement with features afflicting the central and southern basins suggests that mechanisms of recent surface melt are similar to those found throughout the 33 year record. These mechanisms, such as atmospheric blocking, may have become more frequent or more severe in recent years (e.g., Hanna et al. 2015).

5. Summary

A regression analysis has been conducted using GrIS daily basin-scale melt area and anomalies of MERRA-2 variables for atmospheric circulation, cloudiness, and surface radiative fluxes over the period 1980-2012. The analysis is conducted to understand the relation of surface melt to

circulation patterns on sub-monthly time scales, to gain insight on the regional variability of conditions associated with surface melt, and to examine patterns associated with melt over the entirety of the satellite era.

For basins in the southern GrIS, regression patterns indicate a compact high pressure anomaly over the southeastern Greenland bight - to the south of Denmark Strait. Surface melt over northern and northeastern basins are generally associated with low pressure over the central Arctic Ocean. These patterns allow for the northward advection of warm, moist air over the central and western side of the ice sheet. Basin-scale surface melt is generally associated with an enhanced downwelling shortwave flux over eastern edge of the ice sheet, but a decreased shortwave flux and an enhanced downwelling longwave flux over western and southern drainage basins where melt is more prevalent. Spatial heterogeneity is apparent in the patterns. The occurrence of melt events requires blocking to occur at specific locations in order to enhance melt for particular locations on the ice sheet. For basins to the north and east, the direct atmospheric circulation and advection seem less connected to conditions on the ice sheet. For basin 2, there is a suggestion of downslope winds and adiabatic heating that may be associated with melt in the northeast. Melt in northeastern basin 2 has occurred less frequently in the past, and an examination of significant melt events finds differing circulation patterns. The geography does not readily allow for direct heating of the location through advection. In basin 1, the circulation anomalies do not suggest direct advective warming of the ice sheet surface or warming of the atmosphere above the ice sheet. The downwelling longwave regression patterns are consistent with the mechanism described by Bennarz et al., of warm, moist air advecting across the western side of the ice sheet, where longwave energy fluxes are then emitted towards the surface (see also Mattingly et al. 2016). Basin 2 indicates more homogenous longwave

heating over the GrIS, suggesting the need for widespread heating to affect this basin. The downwelling shortwave patterns generally have a meridional character, with western regression values contrasting with eastern values of opposite sign. Negative values are associated with anomalies in the received shortwave flux at the surface, which is indicative of enhanced cloud cover and atmospheric moisture. In agreement with Enderlyn et al. (2014), the consistency of the patterns suggest similar mechanisms are associated with surface melt throughout the time series examined, which extends beyond the significant melt events documented over the last decade. An increased frequency of associated conditions (e.g., Hanna et al. 2015), or enhanced severity of such patterns, are implied reasons for observed trends in recent years.

Acknowledgments

Reanalysis data were obtained from the Goddard Earth Sciences Data and Information Services Center. The MEaSUREs Greenland Surface Melt Daily 25km EASE-Grid 2.0, Version 1 dataset was obtained from the US National Snow and Ice Data Center. This study was funded by a grant from the NASA Interdisciplinary Research in Earth Science (IDS) program. The authors thank three anonymous reviewers for their comments in revising the manuscript.

References

Bacmeister, J.T., M.J. Suarez, and F.R. Robertson, 2006: Rain reevaporation, boundary layer–convection interactions, and Pacific rainfall patterns in an AGCM. *J. Atmos. Sci.*, **63**(12), 3383-3403, doi:10.1175/JAS3791.1.

Bennartz, R., M.D. Shupe, D.D. Turner, V.P. Walden, K. Steffen, C.J. Cox, M.S. Kulie, N.B. Miller, and C. Pettersen, 2013: July 2012 Greenland melt extent enhanced by low-level liquid clouds. *Nature*, **496**(7443), 83-86, doi:10.1038/nature12002.

Bennartz, R., M.D. Shupe, D.D. Turner, V.P. Walden, K. Steffen, C.J. Cox, M.S. Kulie, N.B. Miller, and C. Pettersen, 2013: July 2012 Greenland melt extent enhanced by low-level liquid clouds. *Nature*, **496**(7443), 83-86, doi:10.1038/nature12002.

Box, J.E., X. Fettweis, J.C. Stroeve, M. Tedesco, D.K. Hall, and K. Steffen, 2012: Greenland ice sheet albedo feedback. Thermodynamics and atmospheric drivers. *The Cryosphere*, **6**, 821-839, doi:10.5194/tc-6-821-2012.

Chen, Q., D.H. Bromwich, and L. Bai, 1997: Precipitation over Greenland retrieved by a dynamic method and its relation to cyclonic activity. *J. Climate*, **10**(5), 839-870, doi:10.1175/1520-0442(1997)010<0839:POGRBA>2.0.CO;2.

Chou, M.-D., and M.J. Suarez, 1994: An efficient thermal infrared radiation parameterization for use in general circulation models. Tech. Rpt. Ser. on Global Modeling and Data Assimilation Vol. 3, M.J. Suarez, ed., NASA/TM-1994-104606, NASA Goddard Space Flight Center, Greenbelt, MD, 85 p.

Chou, M.-D., and M.J. Suarez, 1999: A solar radiation parameterization for atmospheric studies. Tech. Rpt. Ser. on Global Modeling and Data Assimilation Vol. 15, M.J. Suarez, ed., NASA/TM-1994-104606, NASA Goddard Space Flight Center, Greenbelt, MD, 38 p.

Colgan, W., J.E. Box, M.L. Andersen, X. Fettweis, B. Csathó, R.S. Fausto, D. Van As, and J. Wahr, 2015: Greenland high-elevation mass balance. Inference and implication of reference period (1961-90) imbalance. *Ann. Glaciol.*, **56**(70), 105-117, doi:10.3189/2015AoG70A967.

469 Cullather, R.I., S.M.J. Nowicki, B. Zhao, and M.J. Suarez, 2014: Evaluation of the surface
 470 representation of the Greenland Ice Sheet in a general circulation model. *J. Climate*, **27**(13),
 471 4835-4856, doi:10.1175/JCLI-D-13-00635.1.

472 Cullather, R.I., S.M.J. Nowicki, B. Zhao, and L.S. Koenig, 2016: A characterization of
 473 Greenland Ice Sheet surface melt and runoff in contemporary reanalyses and a regional
 474 climate model. *Frontiers in Earth Sci.*, **4**, 10, doi:10.3389/feart.2016.00010.

475 Davini, P., C. Cagnazzo, P.G. Fogli, E. Manzini, S. Gualdi, and A. Navarra, 2014: European
 476 blocking and Atlantic jet stream variability in the NCEP/NCAR reanalysis and the CMCC-
 477 CMS climate model. *Clim. Dyn.*, **43**(1), 71-85, doi:10.1007/s00382-013-1873-y.

478 Enderlin, E.M., I.M. Howat, S. Jeong, M.-J. Noh, J.H. van Angelen, and M.R. van den Broeke,
 479 2014: An improved mass budget for the Greenland ice sheet. *Geophys. Res. Lett.*, **41**(3), 866-
 480 872, doi:10.1002/2013GL059010.

481 Fausto, R.S., D. van As, J.E. Box, W. Colgan, P.L. Langen, and R.H. Mottram, 2016: The
 482 implication of nonradiative energy fluxes dominating Greenland ice sheet exceptional
 483 ablation area surface melt in 2012. *Geophys. Res. Lett.*, **43**(6), 2649-2658,
 484 doi:10.1002/2016GL067720.

485 Fettweis, X., G. Mabilhe, M. Erpicum, S. Nicolay, and M. Van den Broeke, 2011: The 1958-2009
 486 Greenland ice sheet surface melt and the mid-tropospheric atmospheric circulation. *Clim.*
 487 *Dyn.*, **36**(1), 139-159, doi:10.1007/s00382-010-0772-8.

488 Folland, C.K., J. Knight, H.W. Linderholm, D. Fereday, S. Ineson, and J.W. Hurrell, 2009: The
 489 summer North Atlantic Oscillation. Past, present, and future. *J. Climate*, **22**(5), 1082-1103,
 490 doi:10.1175/2008JCLI2459.1.

491 Frederiksen, J.S., and R.C. Bell, 1990: North Atlantic blocking during January 1979. Linear
 492 theory. *Quart. J. Roy. Meteor. Soc.*, **116**(496), 1289-1313, doi:10.1002/qj.49711649603.
 493 Gelaro, R., W. McCarty, M.J. Suárez, R. Todling, A. Molod, L. Takacs, C. Randles,
 494 A. Darmenov, M.G. Bosilovich, R. Reichle, K. Wargan, L. Coy, R. Cullather, C. Draper,
 495 S. Akella, V. Buchard, A. Conaty, A. da Silva, W. Gu, G.-K. Kim, R. Koster, R. Lucchesi,
 496 D. Merkova, J.E. Nielsen, G. Partyka, S. Pawson, W. Putman, M. Rienecker, S.D. Schubert,
 497 M. Sienkiewicz, and B. Zhao, 2017: The Modern-Era Retrospective Analysis for Research
 498 and Applications, version 2 (MERRA-2). *J. Climate*, **30**(14), 5419-5454, doi:10.1175/JCLI-
 499 D-16-0758.1.
 500 Global Modeling and Assimilation Office (GMAO), 2015a: MERRA-2 tavg1_2d_slv_Nx: 2d,
 501 Hourly mean, Time-Averaged, Single-Level, Assimilation, Single-Level Diagnostics, version
 502 5.12.4. Goddard Space Flight Center Distributed Active Archive Center (GSFC DAAC),
 503 Greenbelt, Md., doi:10.5067/VJAFPLI1CSIV [Accessed 14-January, 2016].
 504 Global Modeling and Assimilation Office (GMAO), 2015b: MERRA-2 tavg1_2d_rad_Nx: 2d,
 505 Hourly mean, Time-Averaged, Single-Level, Assimilation, Radiation Diagnostics, version
 506 5.12.4. Goddard Space Flight Center Distributed Active Archive Center (GSFC DAAC),
 507 Greenbelt, Md., doi:10.5067/Q9QMY5PBNV1T [Accessed 14-January, 2016].
 508 Global Modeling and Assimilation Office (GMAO), 2015c: MERRA-2 tavg1_2d_flux_Nx: 2d,
 509 Hourly mean, Time-Averaged, Single-Level, Assimilation, Surface Flux Diagnostics, version
 510 5.12.4. Goddard Space Flight Center Distributed Active Archive Center (GSFC DAAC),
 511 Greenbelt, Md., doi:10.5067/7MCPBJ41Y0K6 [Accessed 14-January, 2016].
 512 Global Modeling and Assimilation Office (GMAO), 2015d: MERRA-2 inst3_3d_asm_Np: 2d, 3-
 513 Hourly, Instantaneous, Pressure-Level, Assimilation, Assimilated Meteorological Fields,

version 5.12.4. Goddard Space Flight Center Distributed Active Archive Center (GSFC DAAC), Greenbelt, Md., doi:10.5067/QBZ6MG944HW0 [Accessed 14-January, 2016].

Greuell, W., and T. Konzelmann, 1994: Numerical modelling of the energy balance and englacial temperature of the Greenland Ice Sheet. Calculations for the ETH-Camp location (West Greenland, 1155 m a.s.l.). *Global Planet. Change*, **9**(1-2), 91-114, doi:10.1016/0921-8181(94)90010-8.

Häkkinen, S., D.K. Hall, C.A. Shuman, D.L. Worthen, and N.E. DiGirolamo, 2014: Greenland ice sheet melt from MODIS and associated atmospheric variability. *Geophys. Res. Lett.*, **41**(5), 1600-1607, doi:10.1002/2013GL059185.

Hall, D.K., S.V. Nghiem, C.B. Schaaf, N.E. DiGirolamo, and G. Neumann, 2009: Evaluation of surface and near-surface melt characteristics on the Greenland ice sheet using MODIS and QuikSCAT data. *J. Geophys. Res.*, **114**(4), F04006, doi:10.1029/2009JF001287.

Hanna, E., X. Fettweis, S.H. Mernild, J. Cappelen, M.H. Ribergaard, C.A. Shuman, K. Steffen, L. Wood, and T.L. Mote, 2014: Atmospheric and oceanic climate forcing of the exceptional Greenland ice sheet surface melt in summer 2012. *Int. J. Climatol.*, **34**(4), 1022-1037. doi:10.1002/joc.3743

Hanna, E., T.E. Cropper, P.D. Jones, A.A. Scaife, and R. Allan, 2015: Recent seasonal asymmetric changes in the NAO (a marked summer decline and increased winter variability) and associated changes in the AO and Greenland Blocking Index. *Int. J. Climatol.*, **35**(9), 2540-2554, doi:10.1002/joc.4157.

Hanna, E., T.E. Cropper, R.J. Hall, and J. Cappelen, 2016: Greenland Blocking Index 1851-2015. A regional climate change signal. *Int. J. Climatol.*, **36**(15), 4847-4861. doi:10.1002/joc.4673.

537 Kay, J.E., T. L'Ecuyer, H. Chepfer, N. Loeb, A. Morrison, and G. Cesana, 2016: Recent
 538 advances in Arctic cloud and climate research. *Curr. Clim. Change Rep.*, **2**(4), 159-169,
 539 doi:10.1007/s40641-016-0051-9.

540 Liu, Y., and J.R. Key, 2016. Assessment of Arctic cloud cover anomalies in atmospheric
 541 reanalysis products using satellite data. *J. Climate*, **29**(17), 6065-6083, doi:10.1175/JCLI-D-
 542 15-0861.1.

543 Liu, J., Z. Chen, J. Francis, M. Song, T. Mote, and Y. Hu, 2016: Has Arctic sea ice loss
 544 contributed to increased surface melting of the Greenland Ice Sheet? *J. Climate*, **29**(9), 3373-
 545 3386, doi:10.1175/JCLI-D-15-0391.1.

546 Mattingly, K.S., C.A. Ramseyer, J.J. Rosen, T.L. Mote, and R. Muthyala, 2016: Increasing water
 547 vapor transport to the Greenland Ice Sheet revealed using self-organizing maps. *Geophys.*
 548 *Res. Lett.*, **43**(17), 9250-9258, doi:10.1002/2016GL070424.

549 McLeod, J.T., and T.L. Mote, 2016: Linking interannual variability in extreme Greenland
 550 blocking episodes to the recent increase in summer melting across the Greenland ice sheet.
 551 *Int. J. Climatol.*, **36**(3), 1484-1499, doi:10.1002/joc.4440.

552 Molod, A., 2012: Constraints on the profiles of total water PDF in AGCMs from AIRS and a
 553 high-resolution model. *J. Climate*, **25**(23), 8341-8352, doi:10.1175/JCLI-D-11-00412.1.

554 Molod, A., L. Takacs, M. Suarez, and J. Bacmeister, 2015: Development of the GEOS-5
 555 atmospheric general circulation model. Evolution from MERRA to MERRA2. *Geosci. Model*
 556 *Dev.*, **8**(5), 1339-1356, doi:10.5194/gmd-8-1339-2015.

557 Moore, G.W.K., I.A. Renfrew, and J.J. Cassano, 2013: Greenland plateau jets. *Tellus Ser. A*,
 558 **65**(1), 17468, doi:10.3402/tellusa.v65i0.17468.

559 Mote, T.L., 2007: Greenland surface melt trends 1973–2007: Evidence of a large increase in
 560 2007. *Geophys. Res. Lett.*, **34**(22), L22507, doi:10.1029/2007GL031976.

561 Mote, T. L. 2014: MEaSUREs Greenland Surface Melt Daily 25km EASE-Grid 2.0. NASA
 562 National Snow and Ice Data Center Distributed Active Archive Center, Boulder, Colo.,
 563 doi:10.5067/MEASURES/CRYOSPHERE/nsidc-0533.001 [Accessed 5-January, 2014].

564 Mote, T.L., and M.R. Anderson, 1995: Variations in snowpack melt on the Greenland ice sheet
 565 based on passive-microwave measurements. *J. Glaciol.*, **41**(137), 51-60,
 566 doi:10.3198/1995JoG41-137-51-60.

567 Nghiem, S.V., D.K. Hall, T.L. Mote, M. Tedesco, M.R. Albert, K. Keegan, C.A. Shuman, N.E.
 568 DiGirolamo, and G. Neumann, 2012: The extreme melt across the Greenland ice sheet in
 569 2012. *Geophys. Res. Lett.*, **39**(20), L20502, doi:10.1029/2012GL053611.

570 Noël, B., X. Fettweis, W.J. van de Berg, M.R. van den Broeke, and M. Erpicum, 2014:
 571 Sensitivity of Greenland Ice Sheet surface mass balance to perturbations in sea surface
 572 temperature and sea ice cover. A study with the regional climate model MAR. *The*
 573 *Cryosphere*, **8**, 1871-1883, doi:10.5194/tc-8-1871-2014.

574 Rajewicz, J., and S.J. Marshall, 2014: Variability and trends in anticyclonic circulation over the
 575 Greenland ice sheet, 1948–2013. *Geophys. Res. Lett.*, **41**(8), 2842-2850,
 576 doi:10.1002/2014GL059255.

577 Reeves Eyre, J.E.J., and X. Zeng, 2017: Evaluation of Greenland near surface air temperature
 578 datasets. *The Cryosphere*, **11**(4), 1591-1605, doi:10.5194/tc-11-1591-2017.

579 Rennermalm, A.K., L.C. Smith, J.C. Stroeve, and V.W. Chu, 2009: Does sea ice influence
 580 Greenland ice sheet surface-melt? *Environ. Res. Lett.*, **4**(2), 024011, doi:10.1088/1748-
 581 9326/4/2/024011.

582 Rienecker, M.M., M.J. Suarez, R. Gelaro, R. Todling, J. Bacmeister, E. Liu, M.G. Bosilovich,
 583 S.D. Schubert, L. Takacs, G. Kim, S. Bloom, J. Chen, D. Collins, A. Conaty, A. da Silva, W.
 584 Gu, J. Joiner, R.D. Koster, R. Lucchesi, A. Molod, T. Owens, S. Pawson, P. Pegion, C.R.
 585 Redder, R. Reichle, F.R. Robertson, A.G. Ruddick, M. Sienkiewicz, and J. Woollen, 2011:
 586 MERRA: NASA's Modern-Era Retrospective Analysis for Research and Applications. *J.*
 587 *Climate*, **24**(14), 3624-3648, doi:10.1175/JCLI-D-11-00015.1.

588 Rignot, E., I. Velicogna, M.R. van den Broeke, A. Monaghan, and J. T. M. Lenaerts, 2011:
 589 Acceleration of the contribution of the Greenland and Antarctic ice sheets to sea level rise.
 590 *Geophys. Res. Lett.*, **38**(5), L05503, doi:10.1029/2011GL046583.

591 Robasky, F.M., and D.H. Bromwich, 1994: Greenland precipitation estimates from the
 592 atmospheric moisture budget. *Geophys. Res. Lett.*, **21**(23), 2495-2498,
 593 doi:10.1029/94GL01915.

594 Seo, K.-W., D.E. Waliser, C.-K. Lee, B. Tian, T. Scambos, B.-M. Kim, J.H. van Angelen, and
 595 M.R. van den Broeke, 2015: Accelerated mass loss from Greenland ice sheet: Links to
 596 atmospheric circulation in the North Atlantic. *Global Planet. Change*, **128**, 61-71,
 597 doi:10.1016/j.gloplacha.2015.02.006.

598 Serreze, M.C., J. Stroeve, A.P. Barrett, and L.N. Boisvert, 2016. Summer atmospheric
 599 circulation anomalies over the Arctic Ocean and their influence on September sea ice extent.
 600 A cautionary tale. *J. Geophys. Res.*, **121**(19), 11,463-11,485, doi:10.1002/2016JD025161.

601 Shepherd, A., E.R. Ivins, G. A. V.R. Barletta, M.J. Bentley, S. Bettadpur, K.H. Briggs, D.H.
 602 Bromwich, R. Forsberg, N. Galin, M. Horwath, S. Jacobs, I. Joughin, M.A. King, J.T.M.
 603 Lenaerts, J. Li, S.R.M. Ligtenberg, A. Luckman, S.B. Luthcke, M. McMillan, R. Meister, G.
 604 Milne, J. Mouginot, A. Muir, J.P. Nicolas, J. Paden, A.J. Payne, H. Pritchard, E. Rignot, H.

605 Rott, L.S. Sørensen, T.A. Scambos, B. Scheuchl, E.J.O. Schrama, B. Smith, A.V. Sundal, J.H.
 606 van Angelen, W.J. van de Berg, M.R. van den Broeke, D.G. Vaughan, I. Velicogna, J. Wahr,
 607 P.L. Whitehouse, D.J. Wingham, D. Yi, D. Young, and H.J. Zwally, 2012. A reconciled
 608 estimate of ice-sheet mass balance. *Science*, **338**(6111), 1183-1189,
 609 doi:10.1126/science.1228102.

610 Tedesco, M., X. Fettweis, M.R. van den Broeke, R.S.W. van de Wal, C.J.P.P. Smeets, W.J. van
 611 de Berg, M.C. Serreze, and J.E. Box, 2011: The role of albedo and accumulation in the 2010
 612 melting record in Greenland. *Environ. Res. Lett.*, **6**(1), 014005, doi:10.1088/1748-
 613 9326/6/1/014005.

614 Tedesco, M., X. Fettweis, T. Mote, J. Wahr, P. Alexander, J.E. Box, and B. Wouters, 2013:
 615 Evidence and analysis of 2012 Greenland records from spaceborne observations, a regional
 616 climate model and reanalysis data. *The Cryosphere*, **7**, 615-630, doi:10.5194/tc-7-615-2013.

617 Tedesco, M., T. Mote, X. Fettweis, E. Hanna, J. Jeyaratnam, J.F. Booth, R. Datta, and K. Briggs,
 618 2016a: Arctic cut-off high drives the poleward shift of a new Greenland melting record.
 619 *Nature Commun.*, **7**, 11723, doi:10.1038/ncomms11723.

620 Tedesco, M., S. Doherty, X. Fettweis, P. Alexander, J. Jeyaratnam, and J. Stroeve, 2016b: The
 621 darkening of the Greenland ice sheet: trends, drivers, and projections (1981–2100). *The*
 622 *Cryosphere*, **10**, 477-496, doi:10.5194/tc-10-477-2016.

623 van den Broeke, M.R., J. Bamber, J. Ettema, E. Rignot, E. Schrama, W.J. van de Berg, E. van
 624 Meijgaard, I. Velicogna, and B. Wouters, 2009: Partitioning recent Greenland mass loss.
 625 *Science*, **326**(5955), 984-986, doi:10.1126/science.1178176.

Van Tricht, K., S. Lhermitte, J.T.M. Lenaerts, I.V. Gorodetskaya, T.S. L'Ecuyer, B. Noël, M. R.
 van den Broeke, D.D. Turner, and N.P.M. van Lipzig, 2016: Clouds enhance Greenland ice
 sheet meltwater runoff. *Nature Commun.*, **7**, 10266, doi:10.1038/ncomms10266.
 Velicogna, I., T. C. Sutterley, and M. R. van den Broeke, 2014: Regional acceleration in ice
 mass loss from Greenland and Antarctica using GRACE time-variable gravity data. *J.*
Geophys. Res., **41**(7), 8130-8137, doi:10.1002/2014GL061052.
 Vernon, C.L., J.L. Bamber, J.E. Box, M.R. van den Broeke, X. Fettweis, E. Hanna, and P.
 Huybrechts, 2013: Surface mass balance model intercomparison for the Greenland ice sheet.
The Cryosphere, **7**, 599-614, doi:10.5194/tc-7-599-2013.
 Zwally, H.J., M.B. Giovinetto, M.A. Beckley, and J.L. Saba, 2012: Antarctic and Greenland
 drainage systems. Cryospheric Sciences Laboratory, NASA Goddard Space Flight Center,
 Greenbelt, MD, digital media. [Available online at
http://icesat4.gsfc.nasa.gov/cryo_data/ant_grn_drainage_systems.php.]

List of Figures

1. (a). Greenland surface elevation from Bamber et al. (2001) contoured every 100 m. Boundaries of major GrIS drainage basins of Zwally et al. (2012) are indicated and numbered. (b). Time series of daily melt area derived from passive microwave data (Mote, 2007) corresponding to each basin for the period 1-May 2008 to 1-October 2009. Melt area is expressed as a fraction of the total basin area.
2. Regression of passive microwave-derived daily melt area for basins indicated in green to de-trended MERRA-2 surface temperature anomalies at each grid point for 1980-2012, in °C. The melt area time series is normalized by the total area of the basin and is restricted to values greater than 5 percent of the basin area. The center panel denotes the regression pattern for daily melt area summed over the entire ice sheet. Hatched areas denote regression significance at the 99 percent confidence level.
3. As in Fig. 2, but for de-trended MERRA-2 500 hPa geopotential height anomalies, in geopotential meters.
4. As in Fig. 2, but for de-trended MERRA-2 sea level pressure anomalies, in hPa.
5. As in Fig. 2, but for de-trended MERRA-2 700 hPa temperature anomalies, in °C. Grey shading indicates missing data (the intersection of the 700 hPa level with orography).
6. As in Fig. 2, but for de-trended MERRA-2 surface downwelling longwave radiative flux anomalies, in W m^{-2} .
7. As in Fig. 2, but for de-trended MERRA-2 surface downwelling shortwave radiative flux anomalies, in W m^{-2} .
8. As in Fig. 2, but for de-trended MERRA-2 total cloud fraction anomalies.

9. Regression of passive microwave-derived daily melt area for the total GrIS to de-trended MERRA-2 (a) 10 m zonal wind anomalies and (b) 10 m meridional wind anomalies, in m s^{-1} . Positive values indicate (a) eastward and (b) northward direction. Hatched areas denote regression significance at the 99 percent confidence level.
10. MERRA-2 fields of (a) sea level pressure and 10 m winds, and (b) total cloud fraction for 00:00Z, 11-July 2012. Sea level pressure is contoured every 1 hPa, and wind vectors are shown in m s^{-1} . Cloud fraction is contoured for every 0.05. MEaSUREs surface melt from passive microwave data is indicated with hatching.
11. MERRA-2 fields of (a) sea level pressure and 10 m winds for 00:00Z, 10-July 1989 and 15-July 1989. Sea level pressure is contoured every 1 hPa, and wind vectors are shown in m s^{-1} . MERRA-2 cloud fraction (b) for corresponding dates, contoured for every 0.05. MEaSUREs surface melt from passive microwave data is indicated with hatching.
12. (a) Time series of daily normalized passive microwave-derived melt area for August 1997. Sea level pressure and 10 m winds for (a) 00:00Z, 11-August 1997 and (b) 00:00Z 12 August 1997, contoured every 1 hPa. Wind vectors are shown in m s^{-1} .
13. (a) Time series of daily normalized passive microwave-derived melt area for June/July 2002. Sea level pressure and 10 m winds for (a) 00:00Z, 29-June 2002 and (b) 00:00Z 14-July 2002, contoured every 1 hPa. Wind vectors are shown in m s^{-1} .
14. (a) Time series of fractional basin area delimited by the 0°C isotherm of MERRA-2 skin temperature for the period 1-June to 31-August, 2015. (b) Sea level pressure and 10 m winds for 06:00Z, 02-July 2015, contoured every 1 hPa. Wind vectors are shown in m s^{-1} . (c) Averaged sea level pressure and 10 m winds for July 2015, contoured every 1 hPa.
15. As in Fig. 4, but for the period 1980-1999, in hPa.

687

688 Table 1. Correlation (r) for 1980-2012 time series of daily basin melt area, and area of

689 each basin.

690

	Total GrIS	Basin 1	Basin 2	Basin 3	Basin 4	Basin 5	Basin 6	Basin 7	Basin 8
Total GrIS	1.000								
Basin 1	0.833	1.000							
Basin 2	0.812	0.864	1.000						
Basin 3	0.855	0.671	0.741	1.000					
Basin 4	0.810	0.493	0.502	0.730	1.000				
Basin 5	0.761	0.482	0.444	0.541	0.728	1.000			
Basin 6	0.884	0.598	0.546	0.647	0.762	0.856	1.000		
Basin 7	0.877	0.584	0.595	0.735	0.785	0.656	0.812	1.000	
Basin 8	0.910	0.820	0.752	0.751	0.633	0.590	0.725	0.782	1.000
Area [10^6 km^2]	1.720	0.257	0.326	0.254	0.145	0.051	0.184	0.226	0.276

691

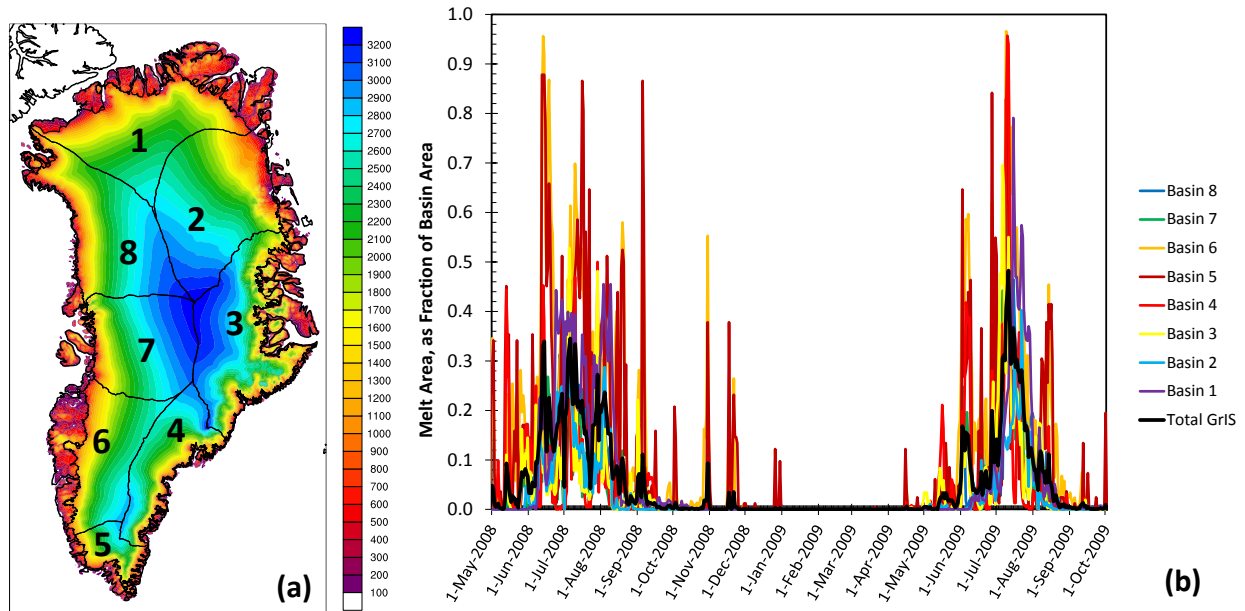


FIGURE 1(a). Greenland surface elevation from Bamber et al. (2001) contoured every 100 m. Boundaries of major GrIS drainage basins of Zwally et al. (2012) are indicated and numbered. (b). Time series of daily melt area derived from passive microwave data (Mote, 2007) corresponding to each basin for the period 1-May 2008 to 1-October 2009. Melt area is expressed as a fraction of the total basin area.

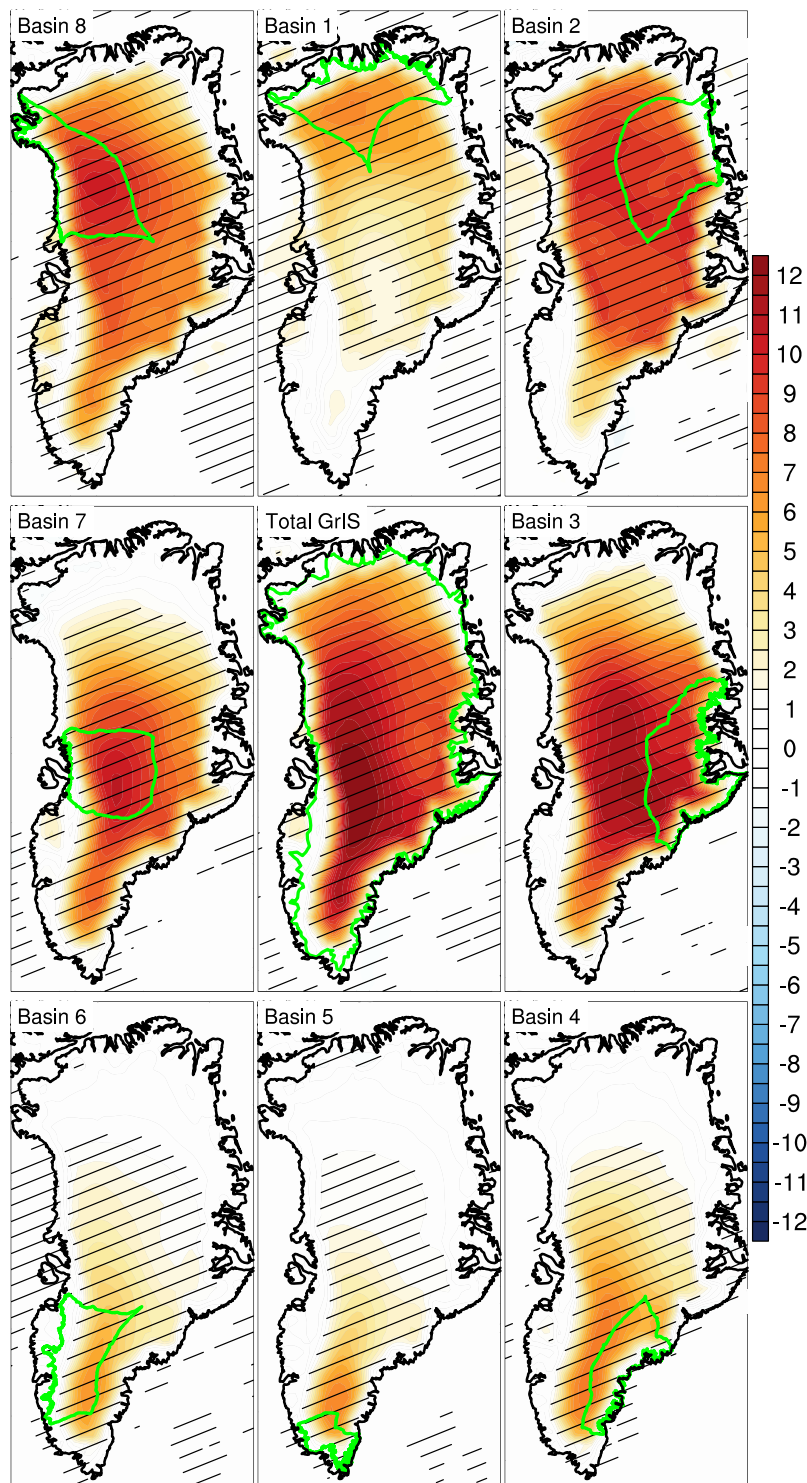


FIGURE 2. Regression of passive microwave-derived daily melt area for basins indicated in green to de-trended MERRA-2 surface temperature anomalies at each grid point for 1980-2012, in $^{\circ}\text{C}$. The melt area time series is normalized by the total area of the basin and is restricted to values greater than 5 percent of the basin area. The center panel denotes the regression pattern for daily melt area summed over the entire ice sheet. Hatched areas denote regression significance at the 99 percent confidence level.

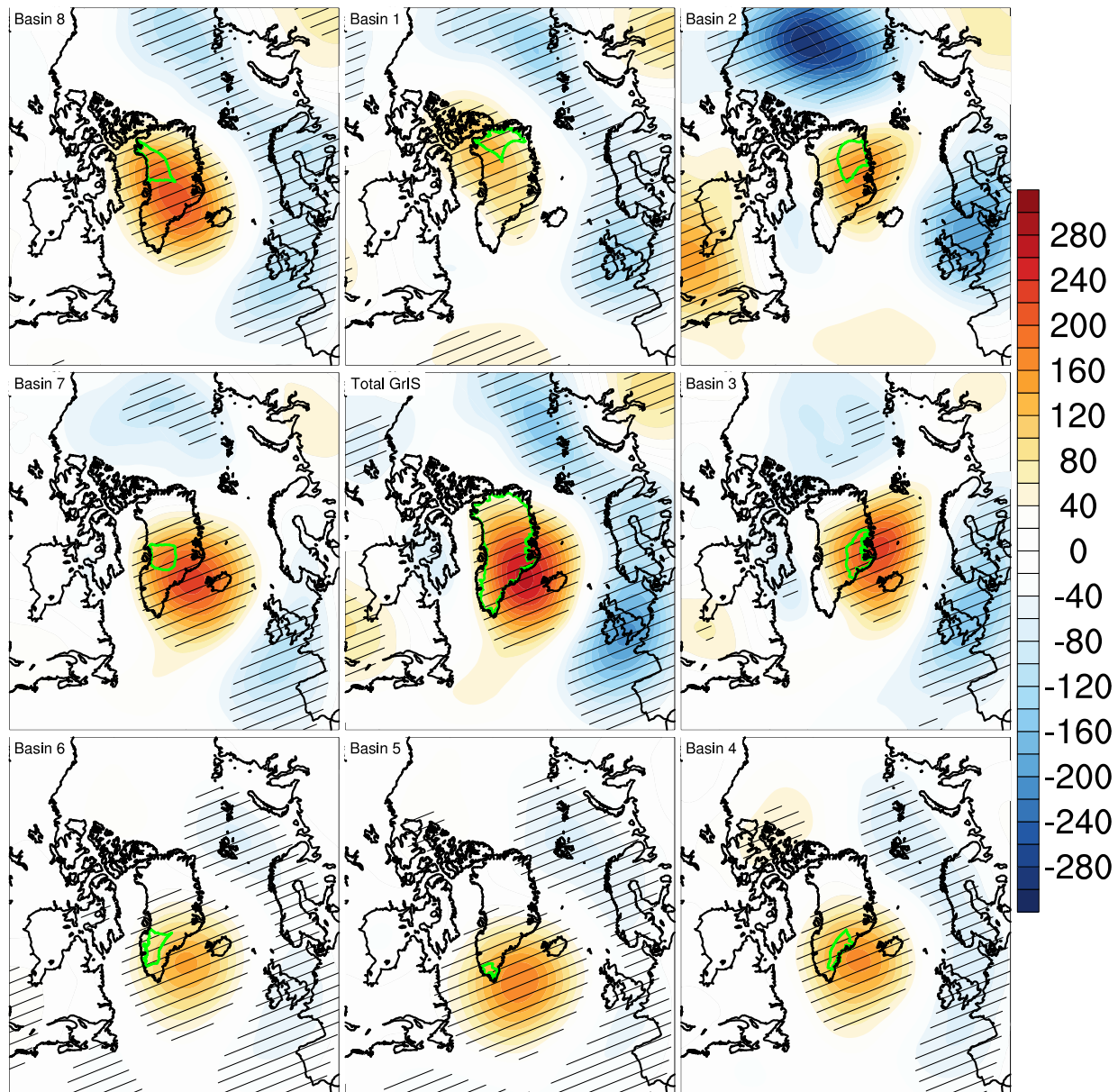


FIGURE 3. As in Fig. 2, but for de-trended MERRA-2 500 hPa geopotential height anomalies, in geopotential meters.

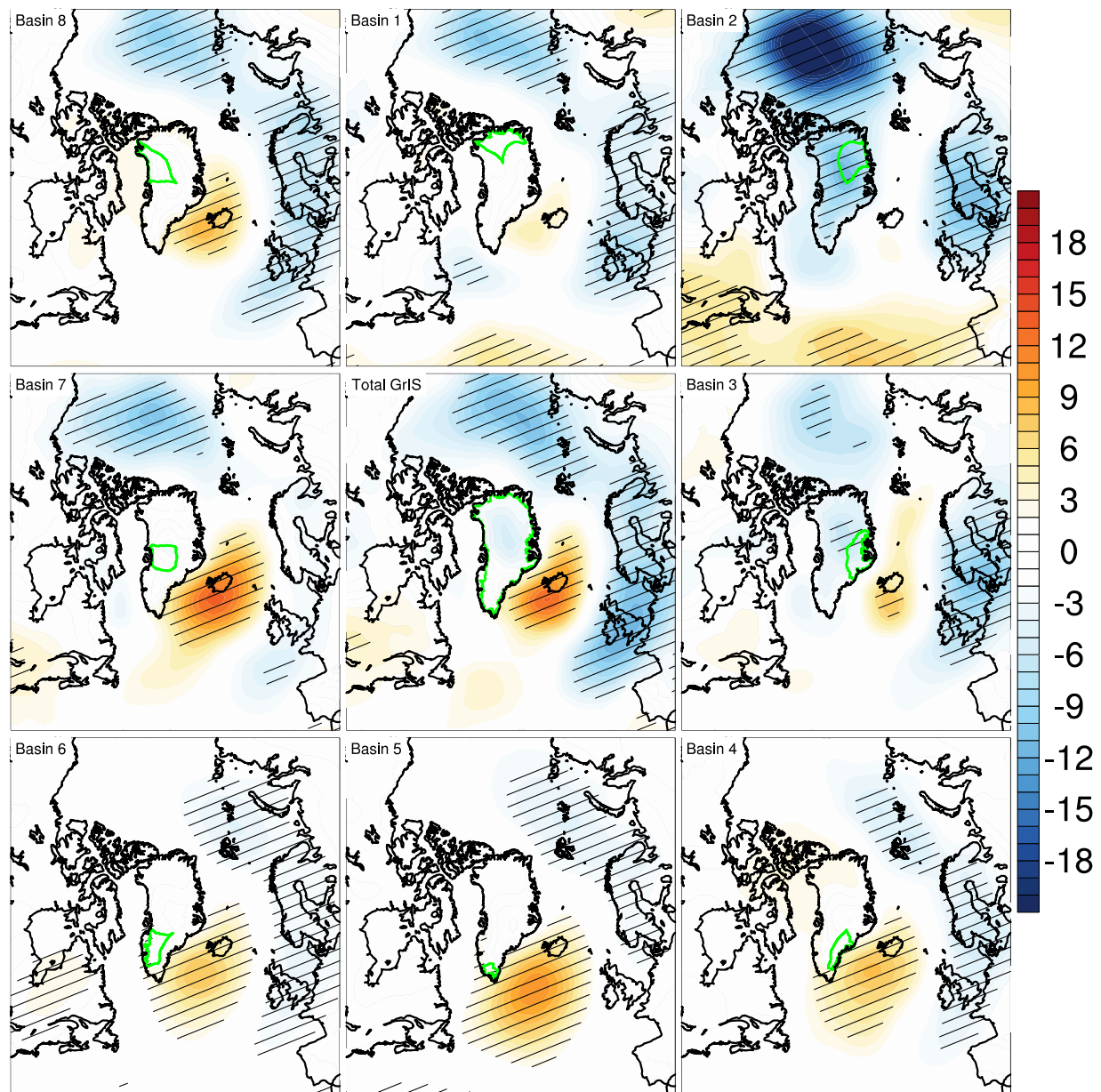


FIGURE 4. As in Fig. 2, but for de-trended MERRA-2 sea level pressure anomalies, in hPa.

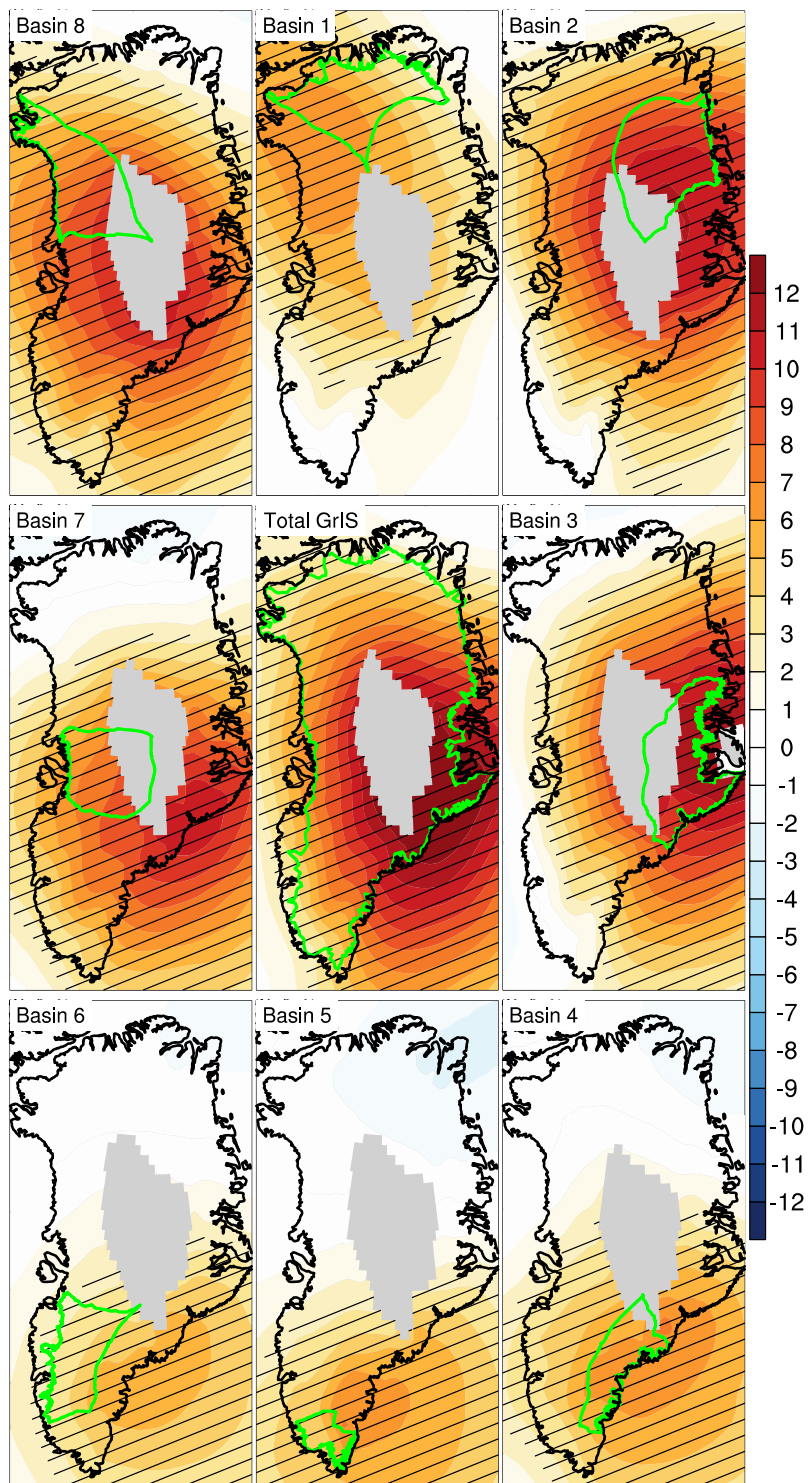


FIGURE 5. As in Fig. 2, but for de-trended MERRA-2 700 hPa temperature anomalies, in °C. Grey shading indicates missing data (the intersection of the 700 hPa level with orography).

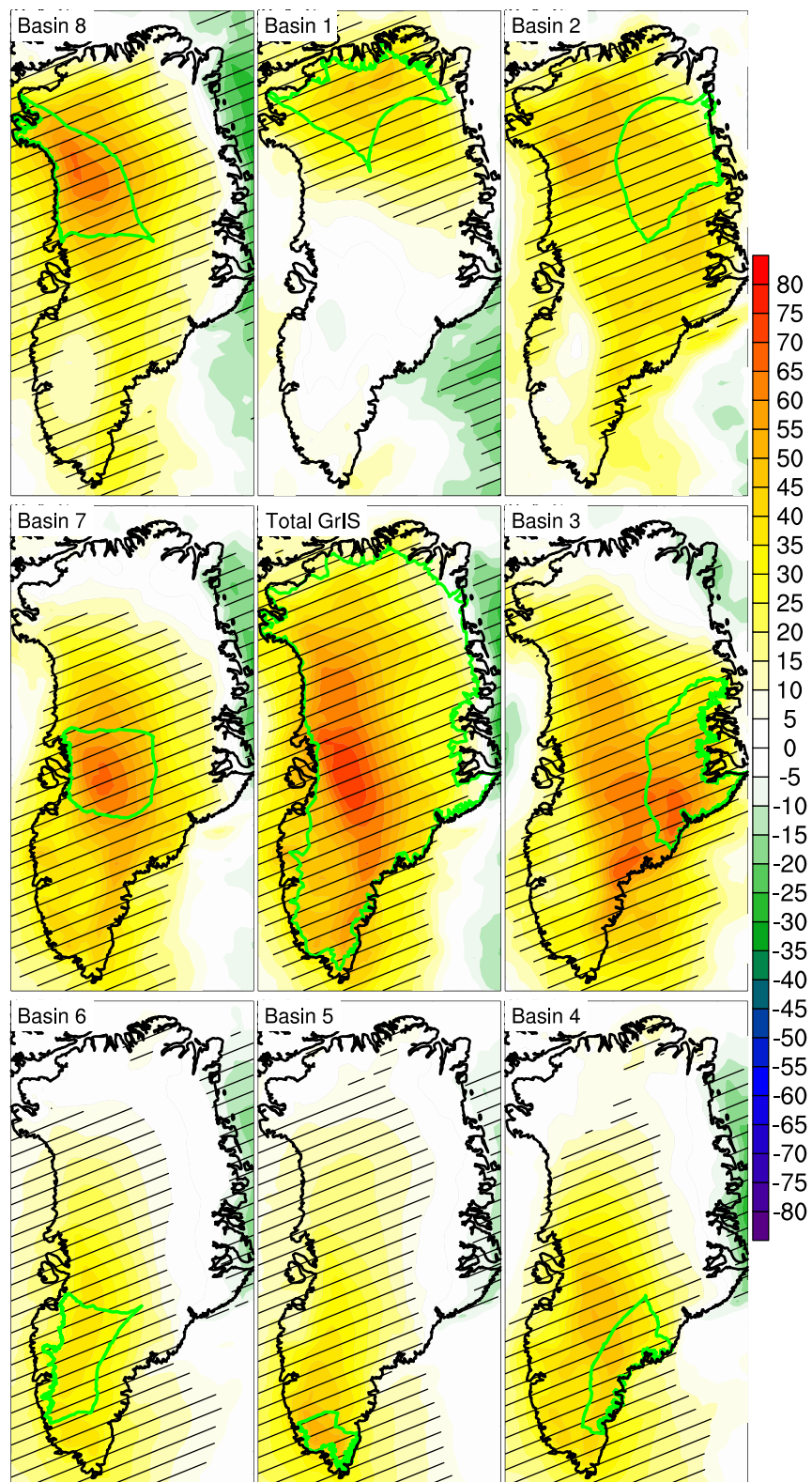


FIGURE 6. As in Fig. 2, but for de-trended MERRA-2 surface downwelling longwave radiative flux anomalies, in W m^{-2} .

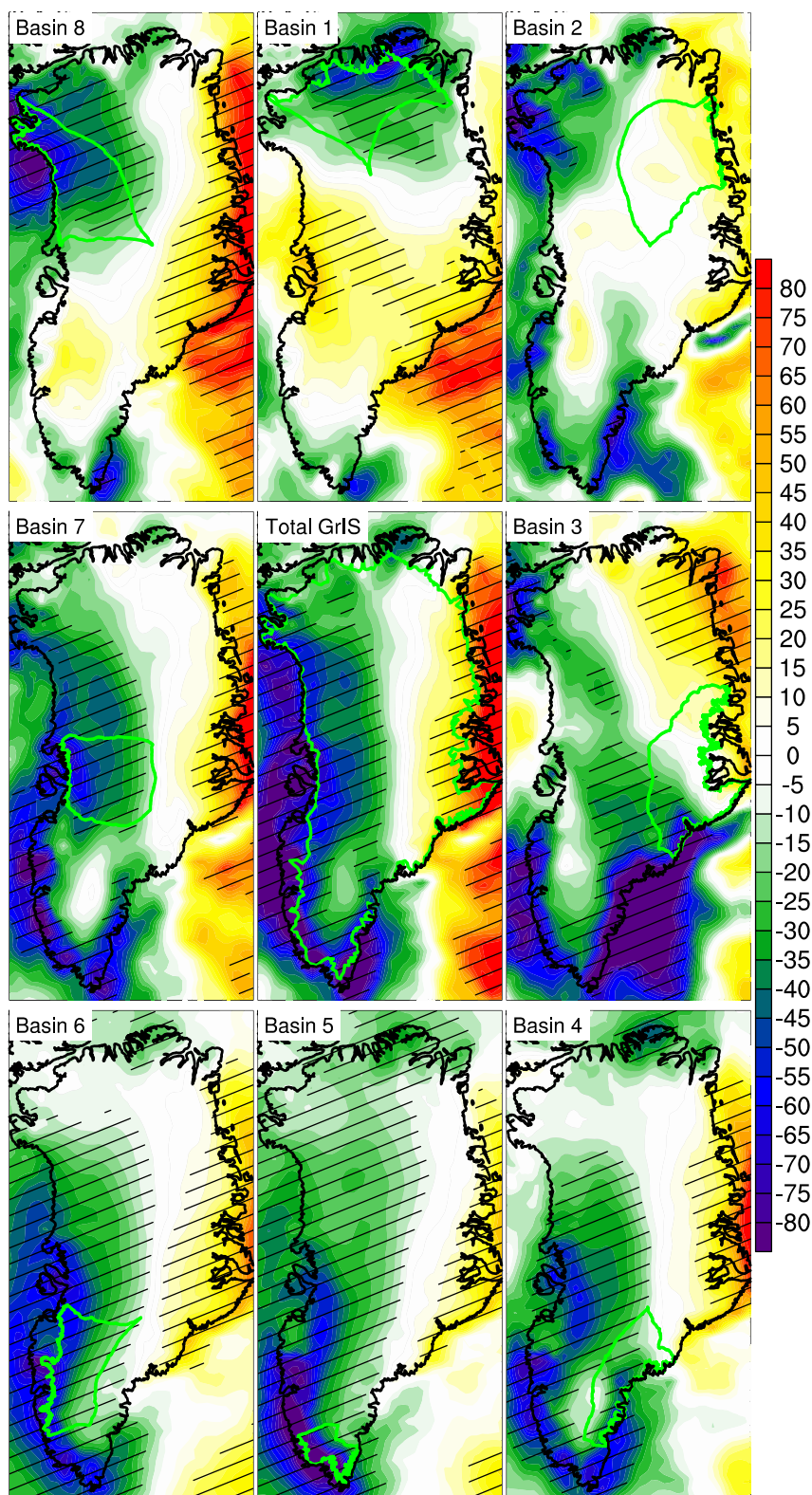


FIGURE 7. As in Fig. 2, but for de-trended MERRA-2 surface downwelling shortwave radiative flux anomalies, in W m^{-2} .

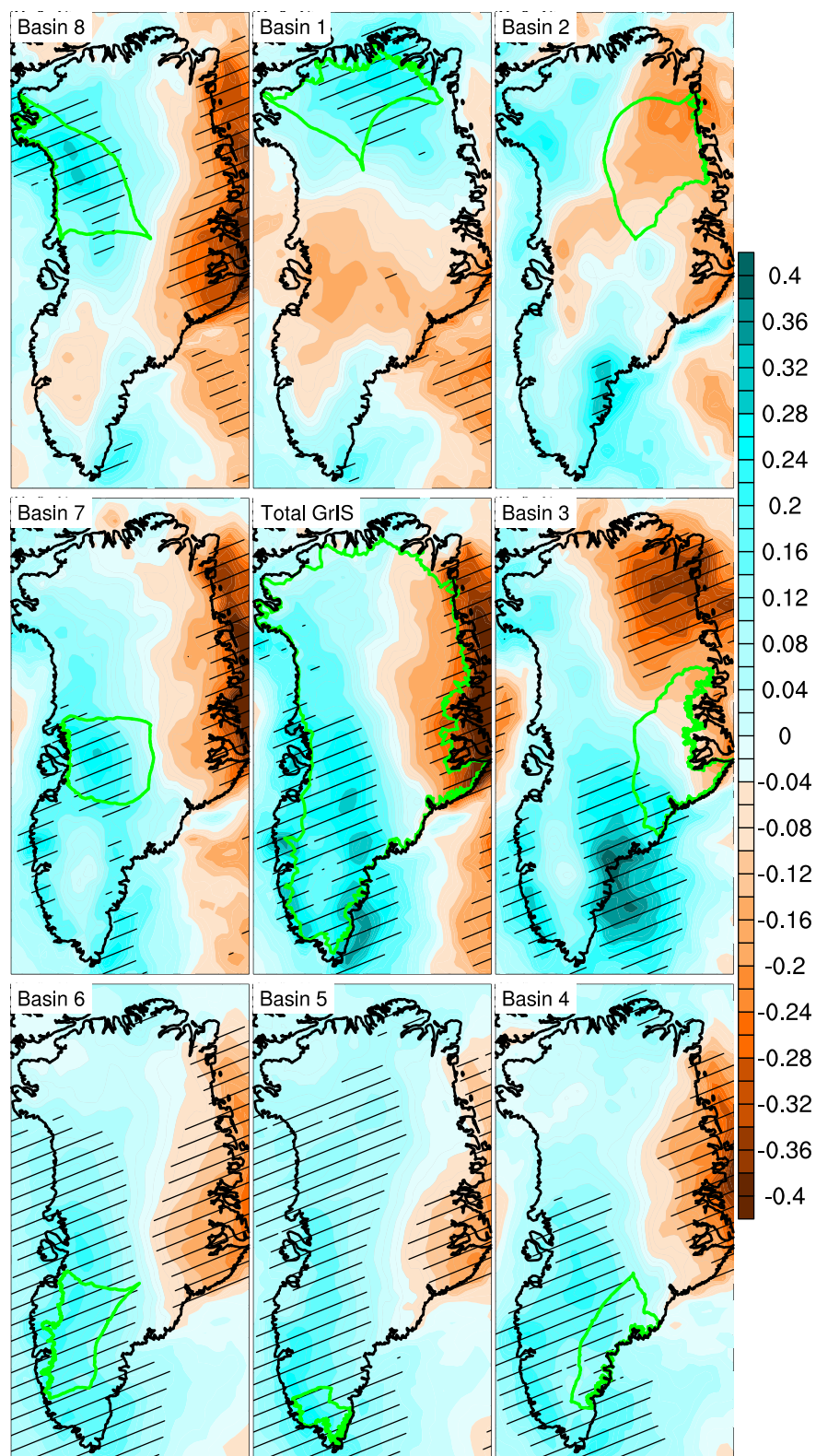


FIGURE 8. As in Fig. 2, but for de-trended MERRA-2 total cloud fraction anomalies.

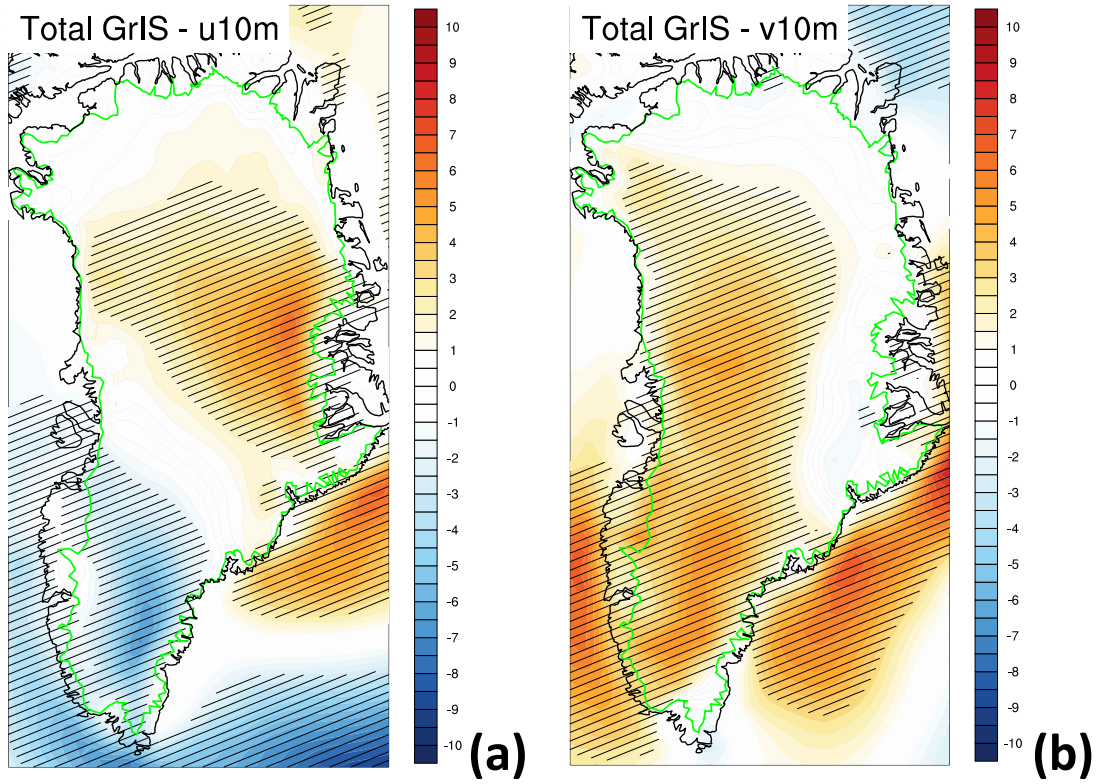


FIGURE 9. Regression of passive microwave-derived daily melt area for the total GrIS to de-trended MERRA-2 (a) 10 m zonal wind anomalies and (b) 10 m meridional wind anomalies, in m s^{-1} . Positive values indicate (a) eastward and (b) northward direction. Hatched areas denote regression significance at the 99 percent confidence level.

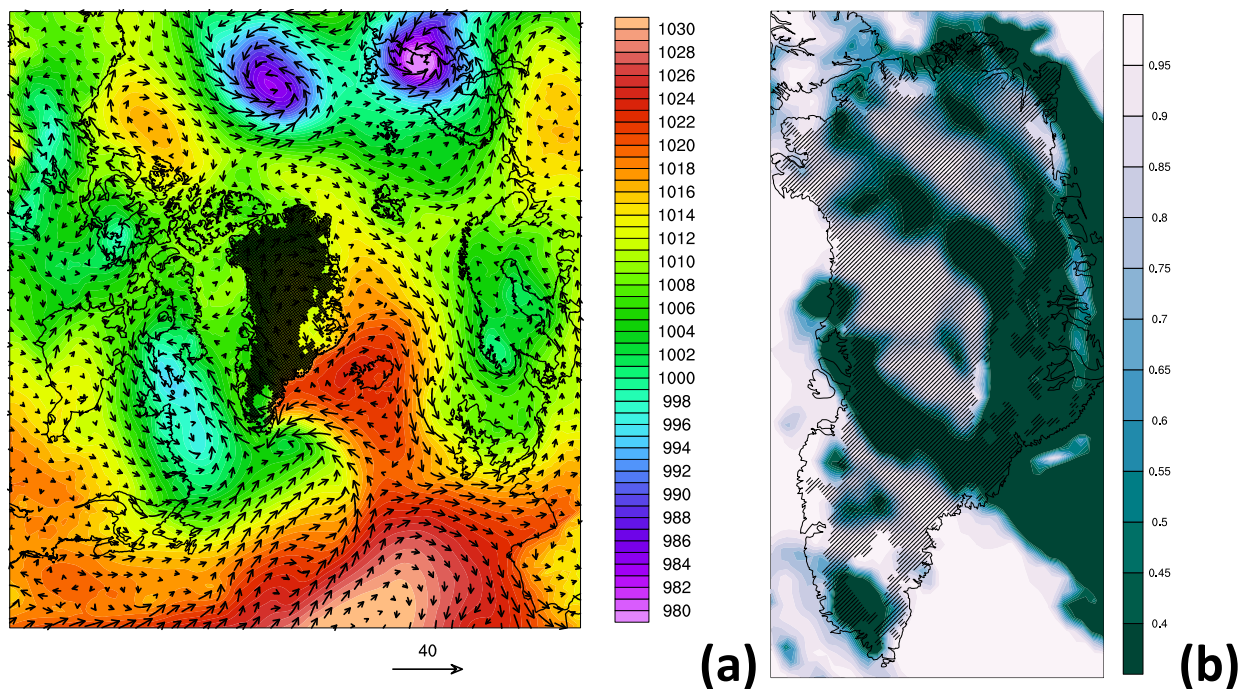


FIGURE 10. MERRA-2 fields of (a) sea level pressure and 10 m winds, and (b) total cloud fraction for 00:00Z, 11-July 2012. Sea level pressure is contoured every 1 hPa, and wind vectors are shown in m s^{-1} . Cloud fraction is contoured for every 0.05. MEaSURES surface melt from passive microwave data is indicated with hatching.

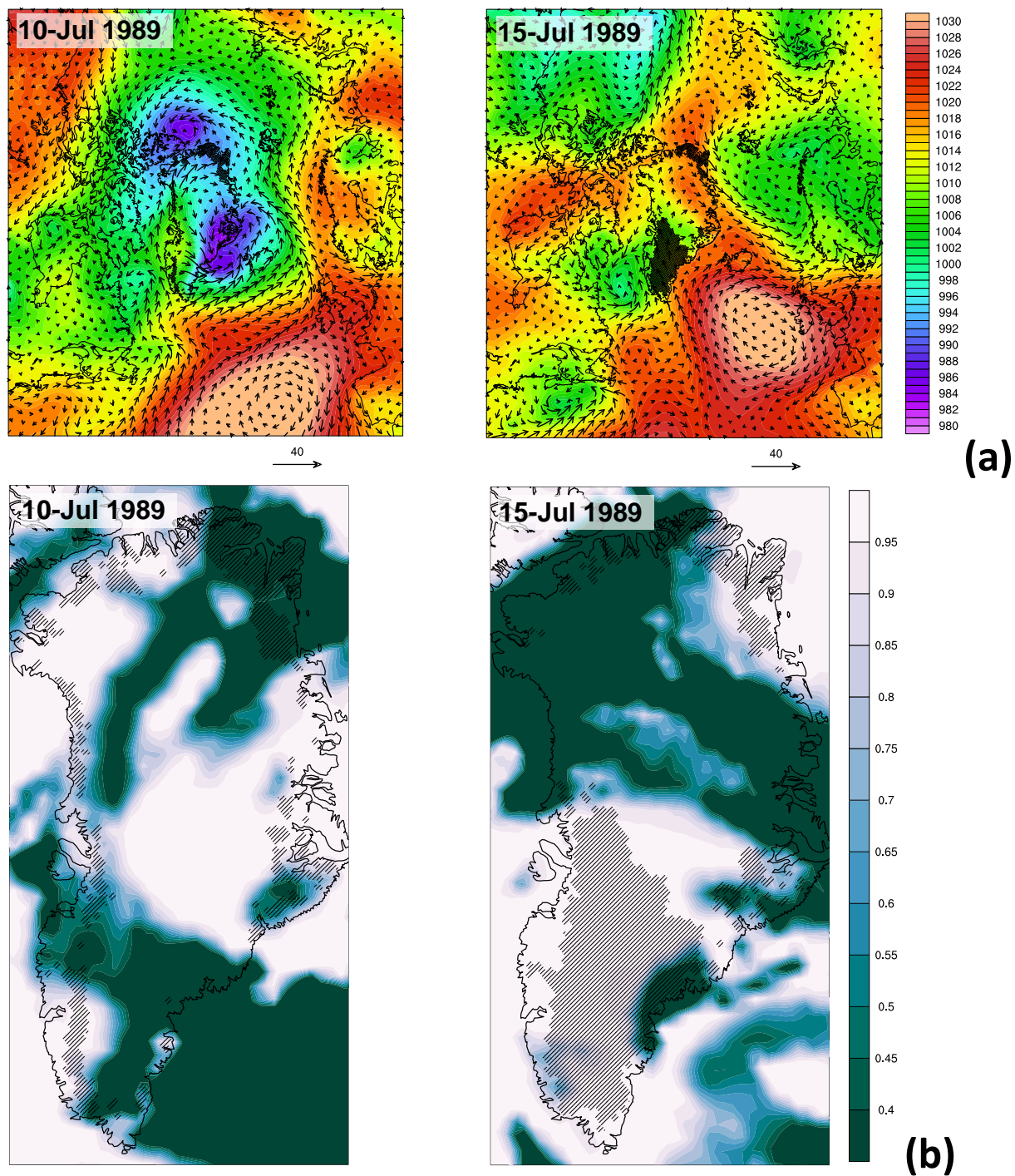


FIGURE 11. MERRA-2 fields of (a) sea level pressure and 10 m winds for 00:00Z, 10-July 1989 and 15-July 1989. Sea level pressure is contoured every 1 hPa, and wind vectors are shown in m s^{-1} . MERRA-2 cloud fraction (b) for corresponding dates, contoured for every 0.05. MEaSUREs surface melt from passive microwave data is indicated with hatching.

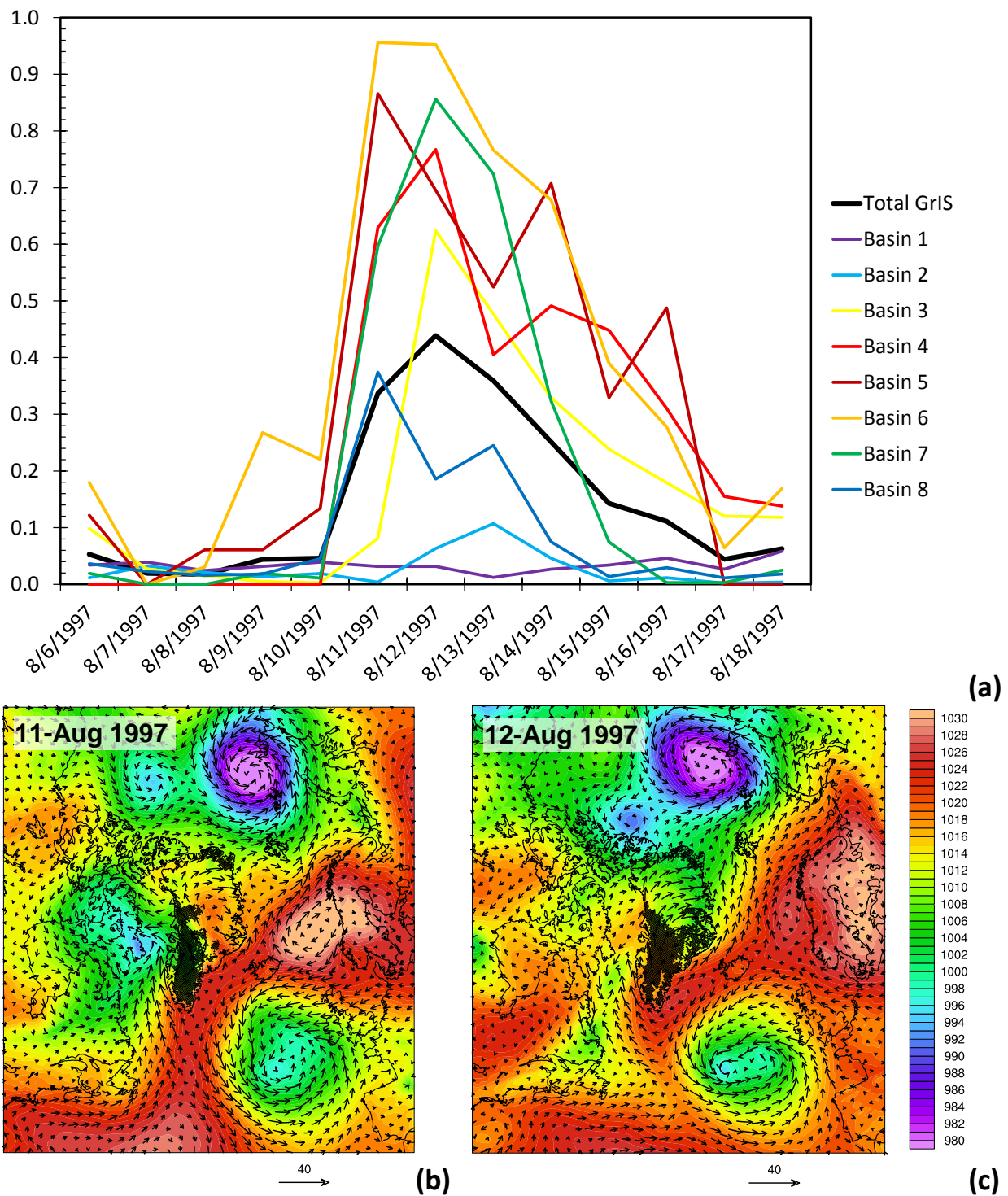


FIGURE 12. (a) Time series of daily normalized passive microwave-derived melt area for August 1997. Sea level pressure and 10 m winds for (a) 00:00Z, 11-August 1997 and (b) 00:00Z 12-August 1997, contoured every 1 hPa. Wind vectors are shown in m s^{-1} .

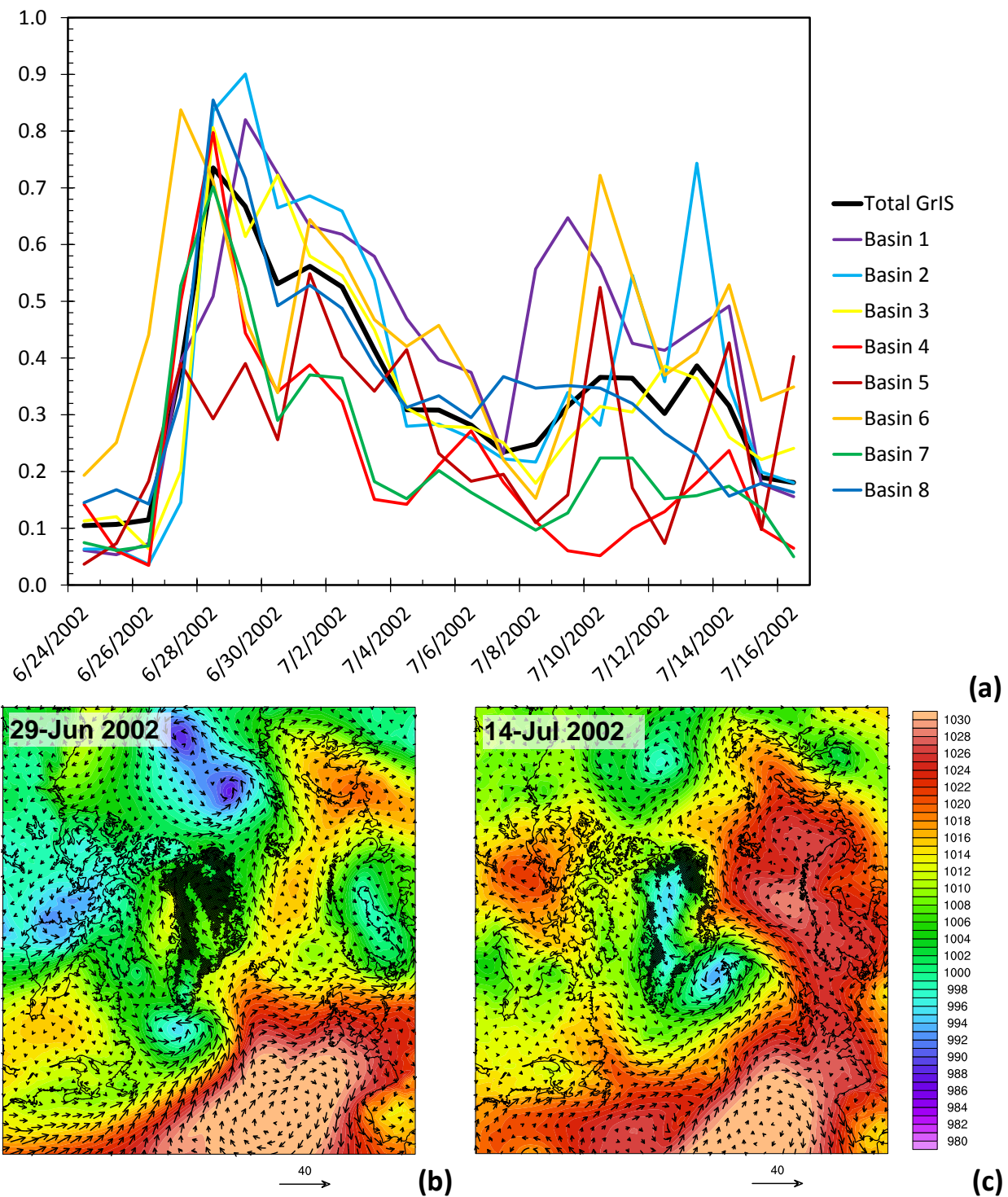
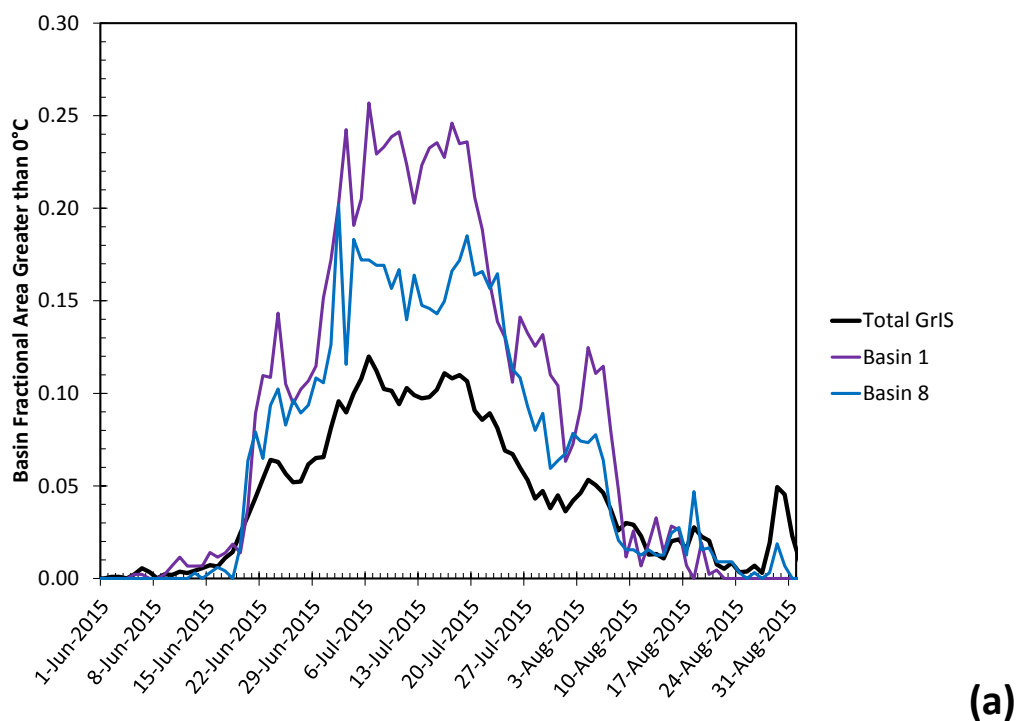
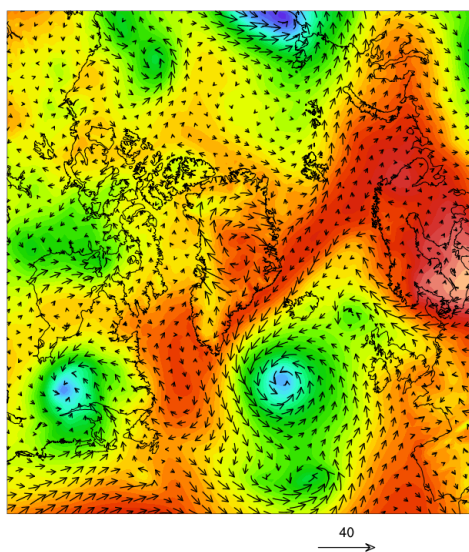


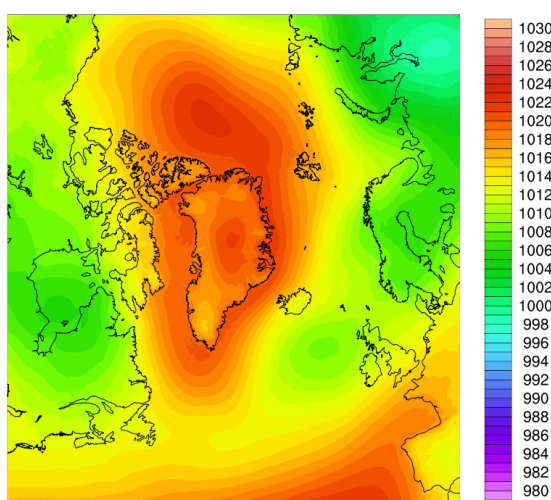
FIGURE 13. (a) Time series of daily normalized passive microwave-derived melt area for June/July 2002. Sea level pressure and 10 m winds for (a) 00:00Z, 29-June 2002 and (b) 00:00Z 14-July 2002, contoured every 1 hPa. Wind vectors are shown in m s^{-1} .



20150702 0630Z



20150701 0030Z



(b)

(c)

FIGURE 14. (a) Time series of fractional basin area delimited by the 0°C isotherm of MERRA-2 skin temperature for the period 1-June to 31-August, 2015. (b) Sea level pressure and 10 m winds for 06:00Z, 02-July 2015, contoured every 1 hPa. Wind vectors are shown in m s^{-1} . (c) Averaged sea level pressure and 10 m winds for July 2015, contoured every 1 hPa.

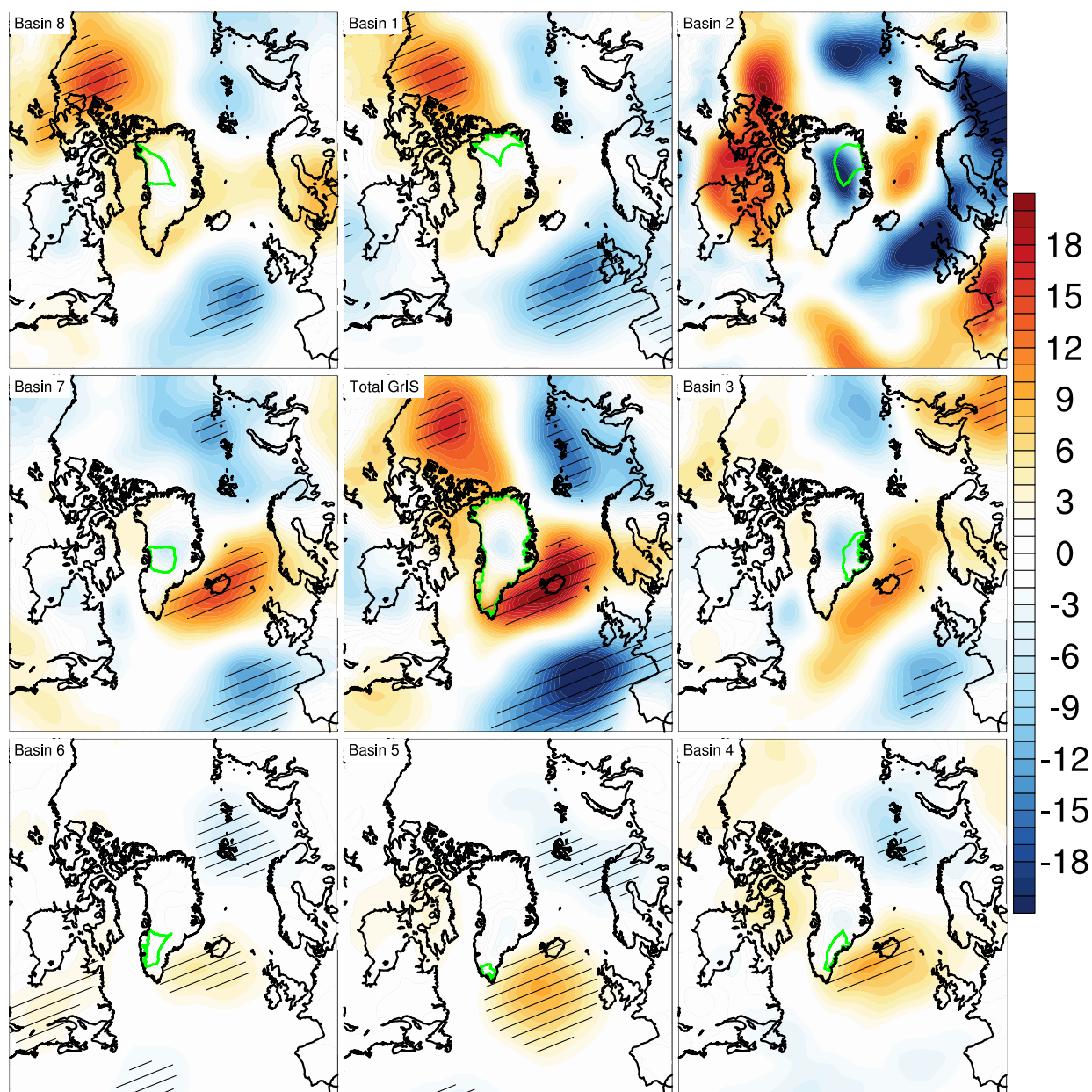


FIGURE 15. As in Fig. 4, but for the period 1980-1999, in hPa.